Powder Technology 427 (2023) 118733

Contents lists available at ScienceDirect

Powder Technology

journal homepage: www.journals.elsevier.com/powder-technology

Ex situ and in situ functionalized Yb/Fe nanoparticles obtained by scanning pulsed laser ablation in liquids: A route to obtain biofunctionalized multiplatform contrast agents for MRI and CT imaging

E. Félix [a,b], J.M. Mánuel [a,b], C. Fernández-Ponce [c,d], M.P. Yeste [b,e], R. Lahoz [f], M.A. Rodríguez [g], I. Abasolo [h,i], M. Llaguno-Munive [h], R. Fernández-Cisnal [d], C. García-Villar [d,j], F. Garcia-Cozar [c,d], R. Litrán [a,b,*], O. Bomati-Miguel [a,b]

[a] Department of Condensed Matter Physics, Faculty of Sciences, University of Cádiz, Puerto Real, 11510 Cádiz, Spain
[b] IMEYMAT: Institute of Research on Electron Microscopy and Materials of the University of Cádiz, Puerto Real, 11510 Cádiz, Spain
[c] Department of Biomedicine, Biotechnology and Public Health, University of Cadiz, Spain
[d] Institute of Biomedical Research Cádiz (INIBICA), Cadiz, Spain
[e] Department of Materials Science and Metallurgic Engineering, and Inorganic Chemistry, Faculty of Sciences, University of Cádiz, Puerto Real, 11510 Cádiz, Spain
[f] Instituto de Nanociencia y Materiales de Aragón (INMA), CSIC-Universidad de Zaragoza, EINA, Edificio Torres Quevedo, María de Luna, 3, 50018 Zaragoza, Spain
[g] Instituto de Cerámica y Vidrio (CSIC), Calle Kelsen, 5, 28049 Madrid, Spain
[h] Drug Delivery & Targeting (DDT) and Functional Validation and Preclinical Research (FVPR) – U20 ICTS Nanbiosis, Vall d'Hebron Institute of Research (VHIR) and Universitat Autònoma de Barcelona (UAB), Passeig de la Vall d'Hebron, 119-129, 08035 Barcelona, Spain
[i] CIBER de Bioingeniería, Biomateriales y Nanomedicina, Instituto de Salud Carlos III, 08035 Barcelona, Spain
[j] Radiology Department, Hospital Universitario Puerta del Mar, Ana de Viya Avenue, n 21, 11009 Cádiz, Spain

HIGHLIGHTS

- Scanning pulsed laser ablation in liquid is used to obtain Yb/Fe nanoparticles.
- Optimization of laser parameters allows to improve the colloidal stability of NPs.
- Functionalized NPs present colloidal stability at physiological pH range.
- The ex situ functionalization route leads to an improvement biocompatibility.
- Resulting NPs are suitable for use as multiplatform contrast agents in MRI and CT.

GRAPHICAL ABSTRACT

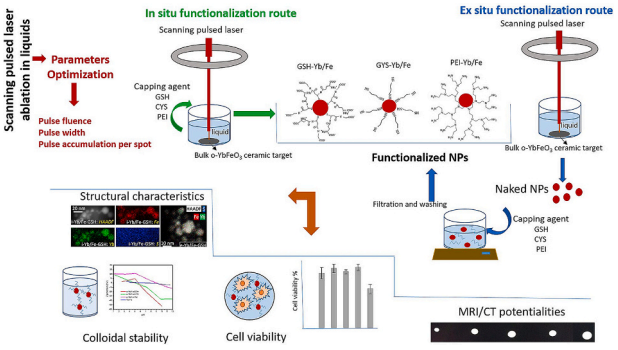

ARTICLE INFO

Keywords:
Laser ablation in liquids
Functionalization
Biocompatible ytterbium/iron nanoparticles
Gluthathione

ABSTRACT

Two distinct strategies were used to improve the colloidal properties of hybrid Yb/Fe oxide NPs previously prepared by the pulsed liquid laser ablation process for use as a contrast agent in medical imaging.

* Corresponding author at: University of Cádiz, Puerto Real, 11510 Cádiz, Spain.
E-mail address: rocio.litran@uca.es (R. Litrán).

https://doi.org/10.1016/j.powtec.2023.118733
Received 27 March 2023; Received in revised form 24 May 2023; Accepted 12 June 2023
Available online 14 June 2023

Cysteamine
Polyethylenimine
Colloidal stability
Multiplatform contrast agents

First, an exhaustive optimization process of the laser ablation synthesis parameters was carried out to reduce the hydrodynamic diameters of the Yb/Fe NPs. The hydrodynamic size was successfully reduced to <200 nm, thereby decreasing the polydispertivity index.

Second, ex situ and in situ functionalization processes using glutathione, cysteamine, or polyethylenimine as capping agents have been developed to increase their colloidal stability at physiological pH values. Transmission electron microscopy, dynamic light scattering, *Z*-potential measurements, and Fourier Transform Infrared spectroscopy were used to examine the structure, morphology, colloidal and surface properties of Yb/Fe NPs.

Colloidal stability of the Yb/Fe NPs as well as the linkage mechanism of functionalization have been studied extensively. This last parameter provides a critical information for subsequently bioconjugations in biomedical applications. Additionally, the biocompatibility of the Yb/Fe NPs was evaluated by MTT (3-(4,5-dimethylthiazol-2-yl)-2,5-diphenyltetrazolium bromide) experiments. These results indicate more appropriate colloidal characteristics and higher biocompatibility for ex situ-functionalized Yb/Fe NPs, especially when the capping agent is glutathione. Additionally, these Yb/Fe NPs show good magnetic resonance imaging and X-ray computerized tomography imaging abilities, thereby indicating promising potential as dual contrast agents.

1. Introduction

Nanoparticles (NPs) for biomedical applications [1], such as diagnostics [2], therapy [3,4], biomarking [5], drug delivery [6,7], and noninvasive imaging techniques [8–10], have been widely studied for several decades [11]. In the field of biomedical imaging, Magnetic Resonance Imaging (MRI) and X-ray computerized tomography (CT) are the most commonly employed techniques to provide anatomical and functional information from inside of the body [12,13]. However, to enhance image contrast to distinguish soft tissues and provide additional functional information, contrast agents (CA) must be used. Conventional iodate systems and Gd^{3+} chelates for CT [14] and MRI [15], respectively, present several disadvantages, such as toxicity, low specificity for the detection of non-vascularized tissues, and low efficiency in some cases [16]. Moreover, a combination of imaging techniques is usually required to achieve more precise diagnoses. Hybrid NPs composed by both, a magnetic phase and a radiopaque phase containing elements with high atomic weights, can be excellent candidates for multi-platform CA [17,18]. Many different routes for NPs synthesis allow obtaining a multiplatform CA that can be simultaneously used in MRI and CT, providing information from both imaging techniques but using a unique CA [19,20].

Ytterbium ferrite hybrid NPs are appropriate candidates for multiplatform CA for medical imaging because of their magnetic and radiopaque features, as well as their low toxicity [20,21]. These hybrid NPs can be synthesized using different bottom-up and top-down methods [22], such as co-precipitation, thermal decomposition, microwave synthesis, or solvothermal synthesis [23,24]. A promising technique for the generation of ytterbium ferrite hybrid NPs is Liquid-Assisted Pulsed Laser Ablation (LA-PLA), which has a probe as an alternative method for the production of NPs, even at the industrial scale [25–27]. LA-PLA is a single-step top-down method in which NPs are synthesized directly in a liquid medium via ablation of massive targets [28–30], which are immersed inside the required solvent [31]. A pulsed laser beam moving across the surface of the bulk target is used to promote ablation [32,33].

We have previously reported results obtained from binary Yb/Fe oxide NPs synthesized by scanning pulsed laser ablation in liquids, starting from an orthorhombic $YbFeO_3$ ceramic bulk target previously sintered [34]. This simple synthesis setup allowed Yb/Fe NPs to have the same composition as the target. In our previous study, two different synthetic routes were used by changing the solvent (distilled water or ethanol) used in the liquid ablation process. Although the solvent used clearly determines both the crystalline structure and magnetic behavior of Yb/Fe NPs, in all cases, this ablation process has provided a successful method to produce colloidal dispersions of Yb/Fe NPs, which exhibited high biocompatibility. The study of magnetic properties revealed that Yb/Fe NPs prepared using ethanol present appropriate features to generate good contrast in MRI images. In addition, these Yb/Fe NPs exhibit suitable X-ray attenuation for use in CT techniques. These characteristics indicate the promising potential of these Yb/Fe NPs for use as CA in multiplatform medical imaging.

However, a fundamental requirement that NPs colloidal dispersions must meet for their potential use in medicine is that they must exhibit hydrodynamic sizes of <200 nm as well as narrow size distributions [35,36]. Although we have achieved this requirement in our previous works, [34] a decrease in the polydispersity index could improve the potential applicability of these NPs in biomedicine [37]. Moreover, NPs should exhibit colloidal stability with appropriate *Z*-potential values, particularly in the physiological pH range [38–40]. A deeper study of the superficial characteristics and colloidal behavior of our NPs must be conducted to improve these features [41–43]. Finally, NPs used in biomedical applications must exhibit low cytotoxicity [44,45] and the possibility of subsequent bioconjugation with other biomolecules [37,38,46]. Surface functionalization is a common strategy not only to promote crosslinking between NPs and specific biological species but also to minimize their cytotoxicity and non-specific binding to biological structures [47]. Functionalization of the NPs surface with species containing bioactive terminal groups, such as amino or carboxylic groups, allows subsequent linking to relevant biomolecules needed for targeted applications [48,49]. NPs functionalization can also contribute to avoiding aggregation, minimizing accumulation in organs, and/or phagocyte activation, thus maintaining a prolonged circulation time [50,51]. This process is especially efficient when ligands are covalently linked to the NP surface. Moreover, functionalization can improve colloidal stability by changing the *Z*-potential value.

In this work, starting from our previous results for Yb/Fe oxide NPs obtained from laser ablation in liquid [34], we implemented an optimization process to obtain Yb/Fe NPs, with hydrodynamic sizes smaller than 200 nm and lower polydispersivity, with the aim of improving Yb/Fe NPs features for biomedical applications [52,53]. Secondly, we functionalized these optimized Yb/Fe NPs developing two different ex situ and in situ functionalization processes, by using three different compounds: GSH (glutathione), CYS (cysteamine), and PEI (polyethyleneimine). We studied the influence of the two functionalization methods, as well as the influence of the species used for coating, on the structural and colloidal properties of the functionalized Yb/Fe nanoparticles, evaluating the colloidal stability by dynamic light scattering (DLS) and *Z*-potential measurements. Using Fourier Transform Infrared spectroscopy (FT-IR), we studied the linkage mechanism by which the molecules are bonded to the Yb/Fe NPs surface. The efficiency of the functionalization process was also evaluated by Transmission Electron Microscopy (TEM). This characterization will allow us to determine whether the capping agent has been properly linked to the Yb/Fe NPs surface, thereby functionalizing it.

Finally, we studied the biocompatibility and efficiency of the functionalized Yb/Fe NPs as MRI/CT CA. Cytotoxicity was studied by analyzing cell viability after incubation with different NPs concentrations to obtain information regarding functionalized Yb/Fe NPs biocompatibility. To evaluate the potential use of these functionalized Yb/Fe NPs as CA, phantoms with different NPs concentrations were

Table 1
Laser irradiation conditions used for the synthesis of Yb/Fe NPs in ethanol.

Sample	Solvent	P [W]	F [kHz]	τ_p [ns]	E_p [mJ]	F [J·cm^{-2}]	v_s [mm·s^{-1}]	N
Yb/Fe-1	EtOH	0.52	25	50	0.021	0.74	125	12
Yb/Fe-2	EtOH	1.87	25	50	0.075	2.64	125	12
Yb/Fe-3*	EtOH	3.40	25	50	0.136	4.81	125	12
Yb/Fe-4	EtOH	3.80	25	50	0.152	5.37	125	12
Yb/Fe-5	EtOH	5.80	25	50	0.232	8.20	125	12
Yb/Fe-6	EtOH	7.83	25	50	0.313	11.08	125	12
Yb/Fe-7	EtOH	3.40	25	50	0.136	4.81	500	3
Yb/Fe-8	EtOH	3.40	25	50	0.136	4.81	1000	2
Yb/Fe-9	EtOH	3.40	25	50	0.136	4.81	1500	1
Yb/Fe-10	EtOH	3.40	10	50	0.340	12.03	125	5
Yb/Fe-11	EtOH	3.40	50	50	0.068	2.41	125	24
Yb/Fe-12	EtOH	3.40	100	50	0.034	1.20	125	48
Yb/Fe-13	EtOH	3.40	200	50	0.017	0.60	125	96
Yb/Fe-14	EtOH	3.40	25	8	0.136	4.81	125	12
Yb/Fe-15	EtOH	3.40	25	20	0.136	4.81	125	12
Yb/Fe-16	EtOH	3.40	25	100	0.136	4.81	125	12
Yb/Fe-17	EtOH	3.40	25	200	0.136	4.81	125	12

P: power of the laser beam. *f*: pulse repetition rate. *τp*: pulse width. *Ep*: average pulse energy. *F*: pulse fluence. v_s: scanning speed. *N*: pulse accumulation per spot. (*) Yb—Fe NPs colloidal dispersion synthesized by using standard laser working parameter referred in [34].

prepared and scanned using clinical-grade MRI and CT. The results demonstrated that the functionalized Yb—Fe NPs exhibited favorable biocompatibility and good signals for dual MR/CT contrast imaging.

2. Experimental

2.1. Materials

Commercial analytical-grade reagents were purchased from Sigma-Aldrich.

2.2. Laser system

The laser used was a commercial high repetition rate pulsed fiber laser emitting at 1064 nm (G4 Pulsed Fiber Laser, model SP-020P-A-EP-Z-A from SPI Lasers). This laser system was equipped with a scanning head equipped with two galvanometric mirrors to control the laser beam trajectory and a f-theta lens of 160 mm of focal distance to give a final laser spot size of aca. 30 μm. The beam movement was controlled with a CAD-like LS-PRO software, allowing an accurate control of the scanning parameters over the target surface. A detailed description of the scanning laser experimental set-up can be consulted in reference. The standard parameters used for the generation of Ytterbium ferrite NPs were:: nominal power (*Pm*) = 20 W, pulse width (*τp*) = 4–200 ns and repetition rate (*f*) = 2 kHz to 1 MkHz,).

2.3. Ytterbium -ferrite nanoparticles synthesis

Colloidal dispersions of Yb ferrite nanoparticles were synthesized by Liquid-Assisted Pulsed Laser Ablation of as-synthesized bulk $YbFeO_3$ ceramic targets placed at the bottom of a Pyrex glass cell containing different solvents. In a previous study, we extensively described ceramic target preparation [34]. In a typical synthesis experiment, a cell containing a $YbFeO_3$ ceramic target and the liquid medium was fitted on a lift platform and placed under a galvanometer scanning head to match the disk surface with the focal distance required for each solvent. Based on our previous results, EtOH (ethanol) were chosen as solvents. The focus distance for each solvent was calculated to maintain the position of the target slightly above the theoretical laser focus to avoid the breakdown of the liquid molecules produced by laser irradiation of the solvent. The solvent column height (5 mm), irradiation time (172 s), laser beam diameter (60 μm), and laser beam wavelength (1064 nm) were fixed based on our previous results. In previous studies, we established the following standard laser working parameters:0.136 mJ for the average laser pulse energy (3.4 W of beam power), 25 kHz for the pulse repetition rate, 50 ns for the pulse width, 4.81 J·cm^{-2} for the pulse fluence, 125 mm•s^{-1} for the scanning speed, 12 for the pulse accumulation per spot (N), and 172 s for the duration of the laser scanning surface process.

The first strategy, followed by the objective of decreasing the hydrodynamic size of Yb/Fe NPs and their size polydispersion, was to optimize the ablation process by studying the influence of laser parameters on the resulting Yb/Fe NPs properties. Thus, the role of parameters such as pulse width (*τp*), repetition rate (*f*), fluence (*F*), pulse number per spot (*N*), and target scanning speed (vs) over the NPs size was analyzed. This allowed optimization of the laser ablation process to obtain NPs with lower hydrodynamic diameters. Consequently, these parameters have been changed to explore their influence on the productivity and characteristics of the as-obtained Yb/Fe NPs colloidal dispersions (see Table 1, samples Yb/Fe-1 to Yb/Fe-17).

2.4. Functionalization

Nevertheless, even with a decrease in hydrodynamic size and polydispersivity, Yb/Fe NPs must exhibit colloidal stability at physiological pH values as well as high biocompatibility. The second strategy is to functionalize the Yb/Fe NPs with the objective of improving colloidal stability, decreasing cytotoxicity, and allowing subsequent bioconjugation with different biomolecules. We used three capping agents to functionalize the Yb/Fe NPs: GSH [37], CYS [38], and PEI [54]. GSH is a tripeptide containing a thiol, two carboxylic, and amine terminal groups, cysteamine is a molecule containing a thiol and an amine terminal groups, and PEI is a polymer with repeating units composed of an amine group and two carbon aliphatic CH_2CH_2 spacers [46,48].

Two different functionalization mechanisms were used to link the capping agent to the Yb/Fe NPs surface. Thus, ex situ functionalized Yb/Fe NPs were obtained by subjecting naked Fe—Yb NPs to a subsequent process of functionalization. However, in situ functionalized Yb/Fe NPs were obtained via a one-pot synthetic route by introducing a capping agent into the aqueous liquid used for the ablation process [55].

2.4.1. In situ functionalization

In situ functionalization was performed during the formation of Yb/Fe NPs by laser ablation, introducing capping agents GSH, CYS, or PEI in the solvent used for the liquid ablation process. Considering that we used hydrophilic molecules to functionalize Yb/Fe NPs and that aqueous solutions are required for biomedical applications, deionized water was used for the ablation process. This procedure allowed us to obtain

capped Yb/Fe NPs via a one-pot method. The as obtained functionalized Yb/Fe NPs were designed using the codes i-GSH-Yb/Fe, i-CYS-Yb/Fe, and i-PEI-Yb/Fe for the Yb/Fe NPs functionalized with GSH, CYS, and PEI, respectively.

2.4.2. Ex situ functionalization

Ex situ functionalization was performed in the second stage of the previously optimized (O-Yb/Fe) NPs obtained after the laser parameters optimization process. Based on our previous results [34], in this case, ethanol was chosen as the solvent for the liquid laser ablation synthesis because Yb/Fe NPs synthesized under EtOH exhibited more appropriate magnetic properties for medical image applications, than their counterparts synthesized in water, as we have previously demonstrated. The O-Yb/Fe NPs obtained from this process were filtered, washed, and subsequently dissolved in 10 mL Milli-Q water containing GSH, CYS, or PEI at a concentration of 10 mg/mL. The dispersions were sonicated in an ultrasonic bath for 30 min, placed on an orbital shaker, and stirred for 8 h. After this process, the resulting Yb/Fe NPs were washed thrice and filtered with a 1:1 mixture of ethanol and water to eliminate the non-linked capping agent. The obtained Yb/Fe NPs were designed using the codes e-GSH-Yb/Fe, e-CYS-Yb/Fe, and e-PEI-Yb/Fe for the Yb/Fe NPs functionalized with GSH, CYS, and PEI, respectively.

2.5. Characterization techniques

2.5.1. Colloidal stability and chemical features

The evaluation of the Fe and Yb concentration ($mg{\cdot}mL^{-1}$) in the Yb/Fe NPs colloidal dispersions was performed via Total Reflection X-ray Fluorescence (TXRF) by using a TXRF 8030c, FEI spectrometer. Moreover, dry weight of the Yb/Fe NPs samples ($mgNPs{\cdot}mL^{-1}$) were performed by measuring, with a high precision microbalance, the weight of the residue obtained, after drying at room temperature, 1 mL of the as-synthesized nanoparticle colloidal dispersions. From these results, the ablation rate ($mg{\cdot}mL^{-1}{\cdot}h^{-1}$) was calculated. To study the colloidal stability of the Yb/Fe NPs before and after the functionalization process, the hydrodynamic size (HD), the overall hydrodynamic polydispersity index (PDI_{HD}) and the Zeta potential in ultrapure water (MQ) were studied. Measurements were performed using dynamic light scattering (DLS; Zetasizer Nano ZS90, Malvern Instruments, equipped with software version 7.10) at 1 mg L^{-1}. The Yb/Fe NPs colloidal dispersions were transferred to a 1.5 mL square cuvette for DLS measurements, performed at 20 °C with samples equilibrated for 2 min before the measurements were started. Fifteen consecutive measurements were collected and averaged to calculate the mean size.

Moreover, Fourier-transform infrared spectroscopy (FTIR) was used to obtain information regarding the link between the capping agent and the Yb/Fe NPs surface. The experiments were recorded with a Bruker Alpha System Spectrophotometer (KBr wafer technique) using the same quantity of sample for all measurements.

2.5.2. Structural and compositional study

The structural and compositional characterization of all synthesized Yb/Fe NPs was also performed using different Transmission Electron Microscopy (TEM)-related techniques. Imaging techniques such as TEM in Diffraction Contrast mode and Bright Field conditions (BFTEM), atomically resolved or high-resolution TEM (HRTEM), and high-angle annular dark-field scanning transmission electron microscopy (HAADF-STEM) allowed us to visualize structural features, such as NPs size or atomic structures. On the other hand, energy dispersive X-ray spectrometry (EDX) has been used to collect the atomic composition on specific areas, as well as to draw compositional maps of areas ranging from few nm^2 up to μm^2. TEM analyses were carried out with a TALOS F200X STEM microscope (Thermo Fisher Scientific, Waltham, MA, USA), operating at a 200 kV accelerating voltage, available at the Servicios Centrales de Investigación Científica y Tecnológica (SC-ICT) facilities, of the University of Cádiz. Samples were prepared by depositing 10 μL of Yb/Fe NPs colloidal solution, which were drop-casted onto a holey-carbon coated Cu grid and dried for five hours. EDX spectra were collected using a Super X G2 XEDS system and analyzed by Velox software. For obtaining the size distributions, around 200 NPs were counted from the TEM images, using the Image J software. The as-obtained particle size distribution was lognormally fitted with parameters μ (natural logarithm of the median diameter) and σ (standard deviation of the natural logarithm of the measured particle sizes). The mean particle diameter (D_{TEM}), the standard deviation (Sd_{DTEM}) and the overall polydispersity index (PDI_{TEM}) of the size distributions were determined according to the following equations.

$$D_{TEM} = exp\left(\mu + \sigma^2/2\right) \quad (1)$$

$$Sd_{DTEM} = exp\left(\mu + \sigma^2/2\right)\sqrt{exp(\sigma^2) - 1} \quad (2)$$

$$PDI_{TEM} = (Sd_{DTEM}/D_{TEM})^2 \quad (3)$$

2.5.3. Cytotoxicity assay and cell culture

Jurkat T cells (American Type Culture Collection, Manassas, VA, USA) were cultured at 37 °C, in a 5% CO_2 atmosphere, in Dulbecco's Modified Eagle's Medium (DMEM) containing 2 mM L-glutamine, 10 mM Hepes, 10% (*v*/v) heat-inactivated fetal bovine serum (FBS), 1% (v/v) non-essential amino acids (NEAA), 1% (v/v) sodium pyruvate, 50 μM 2-mercaptoethanol, 100 U/mL penicillin and 100 μg/mL streptomycin (all from Life Technologies, Carlsbad, CA, USA) [56,57].

2.5.4. Cytotoxicity and cell viability

Jurkat T cells, 5 × 105 cells were cultured in a 48 well plate, in the absence or presence of nanoparticles at 1.5 μg/mL or 15 μg/mL.

Cell viability was analyzed 24 h after the addition of Yb/Fe NPs using an MTT-based assay, as previously described [37]. Briefly, the MTT reactant (Thiazolyl Blue Tetrazolium Bromide, TOX1-1KT, Sigma Aldrich) was added to the cells at a 1:10 ratio (MTT solution/culture medium) and incubated for 3 h at 37 °C. Then, formazan crystals formed inside the cells were dissolved by adding MTT Solubilization Solution (M-8910, Sigma Aldrich) at an amount equivalent to that of the original culture medium with vigorous pipetting. The optical density at 570 nm was evaluated to quantify the amount of formazan crystals, which was proportional to the number of viable cells (background absorbance was measured at 690 nm and subtracted from the 570 nm measurement). Viability was compared to that of untreated controls (100%)). Culture medium in the absence of cells were used as a blank, while cells cultured in the presence of 10% dimethyl sulfoxide (DMSO) were used as a control for decreased cell viability, which was always below 10%. Statistical analysis was performed using Statgraphics software. Significance was determined using ANOVA (analysis of variance) and Multiple Range Tests and Student's *t*-Test.

2.5.5. CT and MRI in vitro measurements

First, in vitro evaluation of the ability to produce contrast in X-ray images of the naked-optimized Yb/Fe NPs colloidal dispersions was conducted by micro-CT analysis. In these experiments, aliquots of aqueous stable colloidal dispersions with different concentrations (from 0.2 $mg_{NPs}{\bullet}mL^{-1}$ to 3.2 $mg_{NPs}{\cdot}mL^{-1}$) were placed into a 96 multiwell cell culture microplate (0.28 mL well) to measure the contrast enhancement produced in images acquire by using a preclinical Quantum FX μCT system by PerkinElmer, Inc. In these analyses, transverse, coronal, and sagittal images of this microplate were recorded using a CT tungsten X-ray tube, working from 30 kV to 90 kV, which is the range of X-ray tube voltages commonly used in CT clinical imaging.

Second, phantoms of functionalized Yb/Fe NPs were prepared in a suite of 1.5 mL tubes to perform in vitro MRI/CT measurements. For this purpose, 50uL of Yb/Fe NPs in deionized water at concentrations of 6.2, 4.65, 3.1, 1.55 mg_{NPs}/mL and 0.775 mg_{NPs}/mL was dispersed by 10 min incubation in an ultrasound water bath (FisherBrand F15052, 140 W).

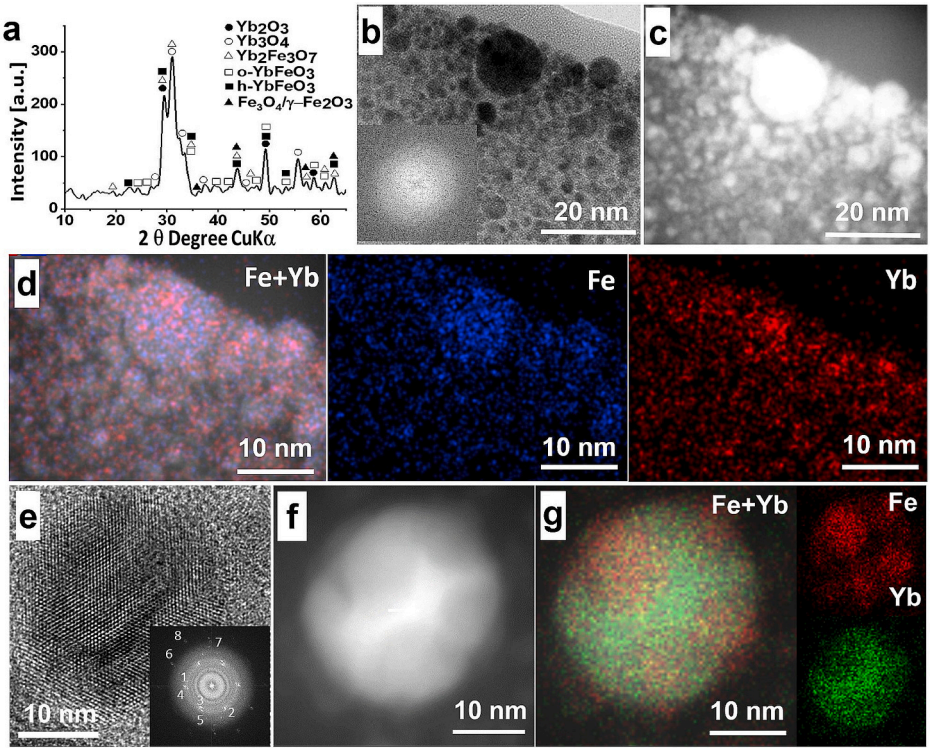

Fig. 1. Structural and compositional characterization of Yb—Fe NPs (sample Yb/Fe-3) synthesized in ETOH via Liquid-Assisted Pulsed Laser Ablation by using starndard laser working parameter reported in E.J. Felix et al. 2023 (power of the laser beam, 3.4 W; pulse repetition rate, 25 KHz; pulse width, 50 ns; average pulse energy, 0.136 mJ; pulse fluence, 4.81 J·cm-2; scanning speed, 125 mms-1; pulse accumulation per spot, 12. a) XRD powder diffractogram of dried Yb/Fe-3 sample. b) Low magnification TEM image of Yb/Fe-3 sample showing Yb—Fe NPs smaller than 15 nm, together with FTT pattern (inset). c) HAADF-STEM image of Yb/Fe NPs showed in image b. d) Compositional Fe and Yb maps of EtOH-NPs smaller than 15 nm displayed in images b and c. e) HRTEM image of an Yb—Fe NPs larger than 20 nm a, together with FTT pattern (inset). f) HAADF-STEM image of large Yb—Fe NPs showed in image e.g) Compositional Fe and Yb map of a large Yb—Fe NPs displayed in images e and f.

Subsequently, 1 mL of a solution containing 30% acrylamide/bisacrylamide 37.5:1 and 0,5% Ammonium Persulfate was added. Samples were vigorously vortexed and 10uL TEMED (tetramethylethylenediamine TEMED) was immediately added to rapidly gelify acrylamide/bisacrylamide.

T2-weigted MRI was performed in vitro using an inversion recovery pulse sequence (Siemens MAGNETOM Tim MRI scanner) at 1.5 T. The experimental conditions were as follows: recycle time (TR) 3500 ms and field of view (FOV) 100 × 100 cm2. In addition, in vitro CT images were acquired using the Revolution EVO EX (General Electric Healthcare).

3. Results and discussion

3.1. Production of Yb/Fe NPs colloidal dispersions by scanning pulsed laser ablation in liquid

3.1.1. Synthesis of NPs using laser standards conditions

Colloidal dispersions of magnetic and radiopaque Yb—Fe based NPs (from this point on named as Yb/Fe-3 sample) were successfully achieved by scanning pulsed laser ablation of handmade orthorhombic $YbFeO_3$ ceramic bulk targets immersed in EtOH, following a synthesis pathway described in previous works [34]. The laser working parameters used in this synthesis (from this point on named as standard conditions): Laser beam power, 3.4 W; pulse repetition rate, 25 KHz; pulse width, 50 ns; average pulse energy, 0.136 mJ; pulse fluence, 4.81 $J{\cdot}cm^{-2}$; scanning speed, 125 $mm{\cdot}s^{-1}$; pulse accumulation per spot, 12.

Powder XRD, HR-TEM, HAADF-STEM, and EDS analysis of these NPs are shown in Fig. 1. The XRD powder diffractogram of the Yb/Fe-3 sample showed a battery of small peaks corresponding to different ytterbium ferrite crystal phases, such as o-$YbFeO_3$, [58] h-$YbFeO_3$ [59] and $Yb_2Fe_3O_7$ [60] and/or ytterbium oxide crystal phases, such as Yb_3O_4 [61] and Yb_2O_3 [62] (see Supplementary Information, Table S.I.T.1). In addition, to a lesser extent, some peaks corresponded to an iron oxide phase with a cubic inverse spinel structure (Fd-3 m) -Fe_2O_3 [63] or Fe_3O_4 [64] (see Supplementary Information, Table S.1.T.2). This result suggests the occurrence of partial decomposition of the ceramic target during the laser ablation process, yielding the subsequent generation of either NPs with different compositions or hybrid NPs formed by different crystalline phases. To further investigate this, the Yb/Fe-3 NPs sample was thoroughly characterized by HR-TEM (Fig. 1b and 1e), and HAADF-STEM (Fig. 1c and 1f), and EDS (see Fig. 1d and 1g).

As shown in Fig. 1b. and 1e, the as-synthesized YbFe-NPs exhibit a roughly spherical morphology, with particle sizes ranging from 3 to 44 nm. In addition, HR-TEM analysis revealed the presence of two populations of Yb—Fe NPs in sample Yb/Fe-3, which exhibited different microstructures: a) poorly crystalline NPs smaller than 10 nm (Fig. 1. b) which did not show crystal lattice fringes; as it was corroborated by the FFTs, which only showed the characteristic rings of the amorphous carbon coating of the Cu TEM grids. b) Population consisting of nanoparticles larger than 20 nm (Fig. 1. e), which clearly shows the presence of well-defined crystal lattice fringes. The high crystallinity of these large NPs was corroborated by their FFT patterns (insert included in Fig. 1. e), which showed several diffraction spots with interplanar distances corresponding to an orthorhombic (Pnma) Yb-ferrite phase-type o-$YbFeO_3$ [58], two ytterbium oxide crystal phases (either an orthorhombic (Pnma) Yb_3O_4 [61], or a cubic (Ia-3) Yb_2O_3 phase [62], and/or a cubic (Fd-3 m) iron oxide phase (either γ-Fe_2O3 [63] or Fe_3O_4 [64]) (see supplementary information, Table S.I.T.2). These findings confirm the polycrystalline nature of these NPs, as observed by XRD analysis. This was also confirmed by the HAADF-STEM analysis (Fig. 1c and 1e), which clearly reveals the presence of abundant bright areas in these NPs in addition to greyish to dark areas within the same NPs, suggesting the presence of areas with different concentrations of Yb or Fe. This was confirmed by the EDS analysis (Fig. 1d and 1g), which showed that although the mean atomic ratio Yb/Fe for each particle varying between 0.66 and 1.05. These elements were irregularly distributed within most of these NPs. Therefore, the white areas in the HAADF-STEM images correspond to highly enriched areas in Yb in the chemical maps, whereas the greyish to dark areas show high Fe content. This partial segregation of Yb and Fe inside the NPs was more evident in large NPs, where the Yb-rich zones in the NP chemical maps (Fig. 1. g) correspond to zones with crystal lattice fringes assigned to the ytterbium oxide phase (either

Table 2
Properties of the Yb/Fe NPs colloidal dispersions synthesized by changing the fluence, width, and repetition rate of the pulse laser, and the scanning speed of the laser beam on the orthorhombic Yb ferrite target surface.

Sample	D_{TEM} [nm]	SdD_{TEM} [nm]	PDI_{TEM}	HD [nm]	PDI_{HD} [nm]	Ablation rate [$mg_{NPs}·mL^{-1}·h^{-1}$]	NPs content [$mg_{NPs}·mL^{-1}$]
Yb/Fe 1	4.6	1.1	0.06	87	0.21	0.04	0.0020
Yb/Fe 2	5.2	1.8	0.12	154	0.23	0.46	0.0218
Yb/Fe 3	7.7	3.4	0.19	172	0.28	0.50	0.0240
Yb/Fe 4	9.4	4.8	0.27	229	0.38	0.80	0.0379
Yb/Fe 5	12.2	6.8	0.31	347	0.44	1.07	0.0511
Yb/Fe 6	15.2	9.3	0.38	508	0.54	1.26	0.0599
Yb/Fe 7	6.5	2.2	0.12	114	0.26	0.41	0.0196
Yb/Fe 8	6.2	1.7	0.08	108	0.24	0.33	0.0160
Yb/Fe 9	6.0	1.4	0.05	85	0.14	0.04	0.0020
Yb/Fe 10	6.6	2.6	0.16	118	0.24	0.39	0.0188
Yb/Fe 11	8.6	4.5	0.27	263	0.37	0.72	0.0348
Yb/Fe 12	9.3	5.7	0.37	450	0.43	1.23	0.0584
Yb/Fe 13	10.9	7.6	0.49	497	0.47	1.52	0.0723
Yb/Fe 14	5.1	1.1	0.05	137	0.21	0.45	0.0214
Yb/Fe 15	7.3	2.9	0.16	160	0.28	0.49	0.0236
Yb/Fe 16	8.8	4.7	0.29	473	0.31	0.97	0.0460
Yb7Fe 17	13.4	10.9	0.66	526	0.70	1.27	0.0611

D_{TEM}: Mean particle diameter. SdD_{TEM}: Standard deviation of the particle size distribution. PDI_{TEM}: Overall polydispersity index of the particle size distribution. HD: hydrodynamic size. PDI_{HD}: overall hydrodynamic polydispersity index.

Yb3O4 or Yb2O3) in the HR-TEM images (Fig. 1e). In contrast, the areas with higher Fe content are roughly related to the interplanar distances of an ytterbium ferrite, either o-$YbFeO_3$ or $Yb_2Fe_3O_7$ (Yb/Fe atomic ratios between 1 and 0.6), and to a lesser extent, to an iron oxide phase, either γ-Fe_2O_3 or Fe_3O_4.

TXRF analysis of Yb/Fe-3 sample revealed Yb and Fe of 0.0150 mg·mL-1 and 0.0049 mg·mL-1, respectively,(Yb/Fe mass ratio of 2.8), being the NPs weight collected after drying of 0.024 mgNPs·mL-1 (ablation rate of 0.50 mgNPs·mL-1·h-1). Yb—Fe NPs in this sample were concentrated by centrifugation at 7.400 rpm and transferred to DW, yielding a slightly dark water stable Yb—Fe NPs colloidal dispersion with HD and PDIHD values of approximately 142 nm and 0.30, respectively. The zeta potential versus pH measurement of the aqueous Yb/Fe-3 colloidal dispersion (data not shown) yielded an isoelectric point of approximately 6.5.

The results show the ability of the synthesis method to produce NPs with appropriate hydrodynamic sizes for biomedical applications in a reproducible manner. However, the polydispersity of NPs, as well as their colloidal stability in the physiological pH range, can be improved. In this regard, we have followed two optimization strategies. The first is to study the influence of laser ablation parameters on the characteristics of the nanoparticles in an attempt to determine the optimal working conditions. Second, the surface characteristics of the nanoparticles were modified through functionalization.

3.1.2. Influence of laser parameters in the properties of Yb/Fe NPs synthetized using ethanol as liquid ablation medium

In order to find the optimal laser parameters, that allow to obtain in a reproducible way Yb/Fe NPs colloidal dispersions with the adequate HD (< 200 nm) and PDIHD (< 0.4) the influence of the pulse width, repetition rate, fluence, pulse number per spot, and target scanning speed over these characteristics was analyzed. This optimization process has been performed using ethanol as liquid in the ablation process, because, according to the above results, biocompatible magnetic and radiopaque Yb/Fe NPs are directly produced with this solvent [34]. Then, the obtained Yb/Fe NPs are named by the code Yb/Fe. The *F*, *τp*, *f*, and vs values were systematically changed one by one, whereas the rest of the laser working parameters remained fixed with respect to those used by us for the synthesis of Yb/Fe NPs under EtOH in our previous work (sample Yb/Fe-3). [34]. Table 2 and Fig. 2 summarize the effect of these variations on the final properties of the as-synthesized Yb/Fe NPs colloidal dispersions.

3.1.2.1. Pulse fluence. The influence of the laser pulse fluence (*F*) was firstly studied by increasing it from 2.64 $J·cm^{-2}$ (sample Yb/Fe-1) to 11.08 $J·cm^{-2}$ (Yb/Fe-6) through variation of the laser beam power from 0.52 W (*Ep* = 0.021 mJ) to 7.83 W (*Ep* = 0.313 mJ) (see Table 1). The TEM analysis of the as-synthesized Yb/Fe NPs (see Supplementary Information, Figs. S.I·F.1 a to S.I·F.1 d) and DLS analysis of samples transferred to DW, revealed that this increase of *F* yielded to an increment in the D_{TEM} and HD values from 4,60 nm to 15.2 nm and from 87 nm to 508 nm, respectively. This also happened for the PDI_{TEM} and PDI_{HD} values, which varied from 0.06 to 0.38 and from 0.14 to 0.54, respectively (see Table 2 and Fig. 2). Moreover, the use of higher laser pulse fluence values leaded also to an increase of the Yb/Fe NPs concentrations of colloidal dispersions from 0.0002 $mg_{NPs}·mL^{-1}$ to 0.0599 $mg_{NPs}·mL^{-1}$ (and in the ablation rate from 0.04 $mg_{NPs}·mL^{-1}·h^{-1}$ to 1.26 $mg_{NPs}·mL^{-1}·h^{-1}$). These results agree with those previously found by other authors [65,66].

TXRF analysis yielded Yb/Fe mass ratios around 3.2 ± 0.3 for the as-synthesized colloidal dispersions. On the other hand, punctual EDS analysis of several Yb/Fe NPs (data not shown) revealed that, in all these samples, most of the NPs presented Yb/Fe atomic ratios from 0.7 to 0.99; whereas a slight enrichment in Yb were observed in the larger NPs, showing Yb/Fe atomic ratios between 0.97 and 1.13. Moreover, HAADF-STEM images and chemical spectra and maps were obtained by EDX (see Supplementary Information, figs. S.I.F.1.f and S.I.F.1.g) revealed that in all cases, Yb and Fe were non-homogeneously distributed in the NP cores. Formation of Fe and Yb rich separated regions or Yb is observed (corresponding to areas with low and high intensity in HAADF images), in accordance with the results already published for EtOH-NPs3. This partial segregation is seen more clearly in the Yb/Fe NPs synthesized using high F values (see supplementary information, fig. S.I.F.1.g); which might be related to the increase in the particle size observed. It is important to note that in the case of the samples synthesized at the lowest F values, some particles formed almost exclusively by Yb (Yb/Fe atomic ratio higher than 8 was observed).

3.1.2.2. Pulse width. The effect of the pulse width on the characteristics of the Yb/Fe NPs colloidal dispersions was also evaluated by changing the pulse width from 8 ns (Sample Yb/Fe-14) to 200 ns (Yb/Fe-17) (see Table 1). Thus, it was found that the increase in *τp* yielded similar variations in the colloidal dispersions to those achieved by changing *F* (Table 2 and Fig. 2). Thus, the increase in *τp* values implied that an increase resulted in progressive growth of the D_{TEM} (see Supplementary Information, Figs. S.I.F.2.a to S.I.F2.d) and HD values from 5.1 nm to

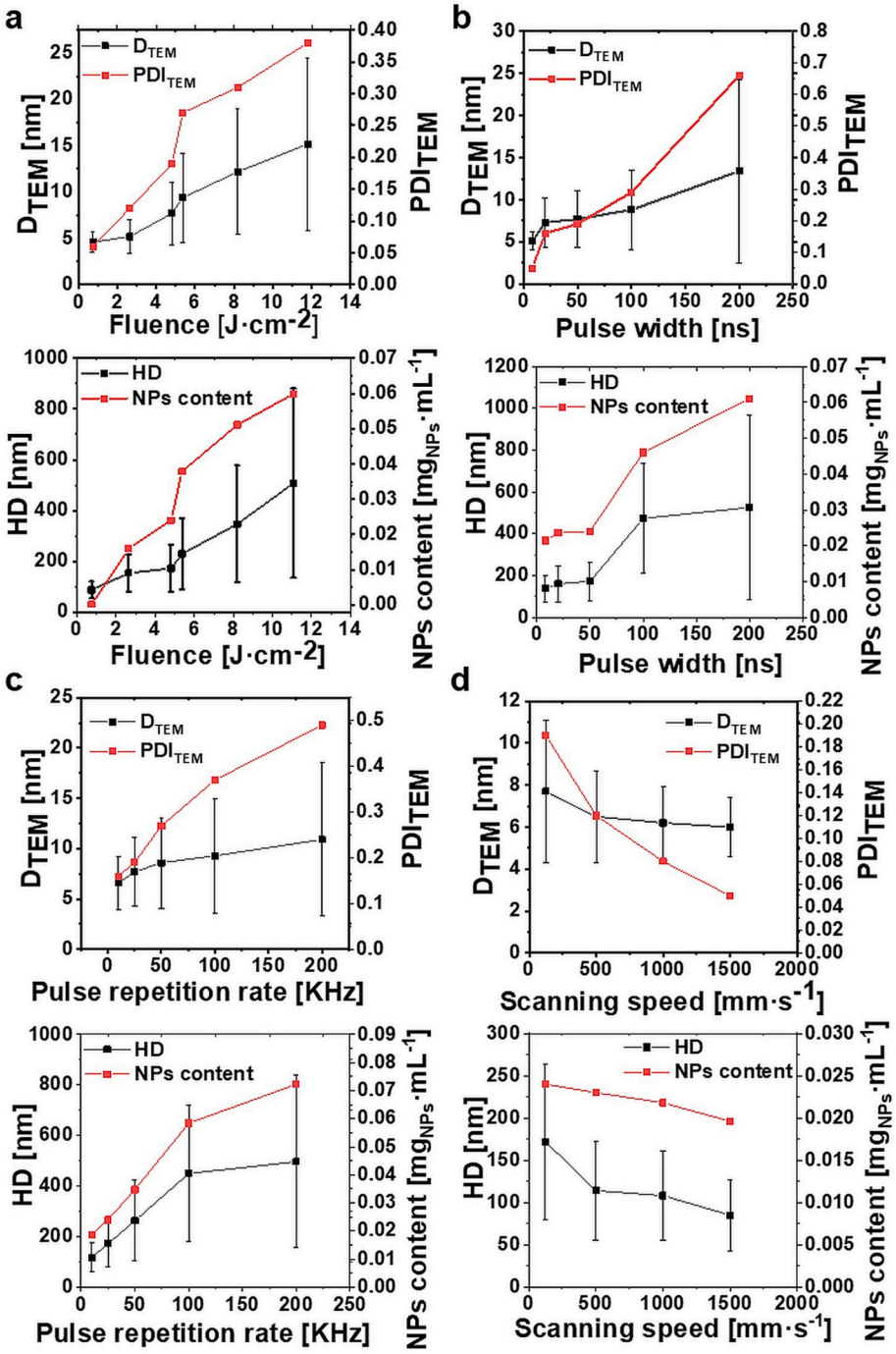

Fig. 2. Effect of laser processing variables on NPs size and productivity: (a) fluence (Samples 1–6); (b) pulse width (Samples 3, 14–17); (c) pulse repetition rate (Samples 3, 10–13); and (d) scanning speed (Samples 3, 7–9). The bars represent standard deviations.

13.4 nm and from 137 nm to 526 nm, respectively. Additionally, a widening of the width of the particle size distribution was observed, calculating PDI_{TEM} and PDI_{HD} values from 0.05 to 0.66 and from 0.21 to 0.70, respectively. A rise in the Yb/Fe NPs concentration from 0.0214 $mg_{NPs}·mL^{-1}$ (ablation rate ≈ 0.45 $mg_{NPs}·mL^{-1}·h^{-1}$) to 0.0611 $mg_{NPs}·mL^{-1}$ ($mg_{NPs}·mL^{-1}·h^{-1}$) was also observed. These results were consistent with those previously reported in the literature [32,66]. Moreover, Yb/Fe mass ratios around 3.3 ± 0.2 were measured by TXRF analysis for these colloidal dispersions. On the other hand, punctual EDS analysis of these samples (data not shown) yielded to Yb/Fe atomic ratios ranging from 0.69 to 0.97 in most of the as synthesized NPs, although a slight enrichment in Yb is also observed in the larger Yb/Fe NPs; which shower Yb/Fe atomic ratios from 0.99 to 1.3. HAADF-STEM images and chemical maps obtained by EDS analysis of these Yb/Fe NPs (see Supplementary Information, Figs. S.I.F.2.e and S.I.F.2.f) showed that, in all cases, these samples were mainly composed of heterogeneous NPs, where the presence of areas enriched in Yb or Fe inside the same nano-construct was more evident as the particle size increased. Similar to the Yb/Fe NPs synthesized using low F values, a small population of NPs formed mainly by Yb was found in the samples synthesized at τp <20 ns.

3.1.2.3. Pulse accumulation per spot. The influence of the applied pulse accumulation per spot value was analyzed by: i) modifying the pulse

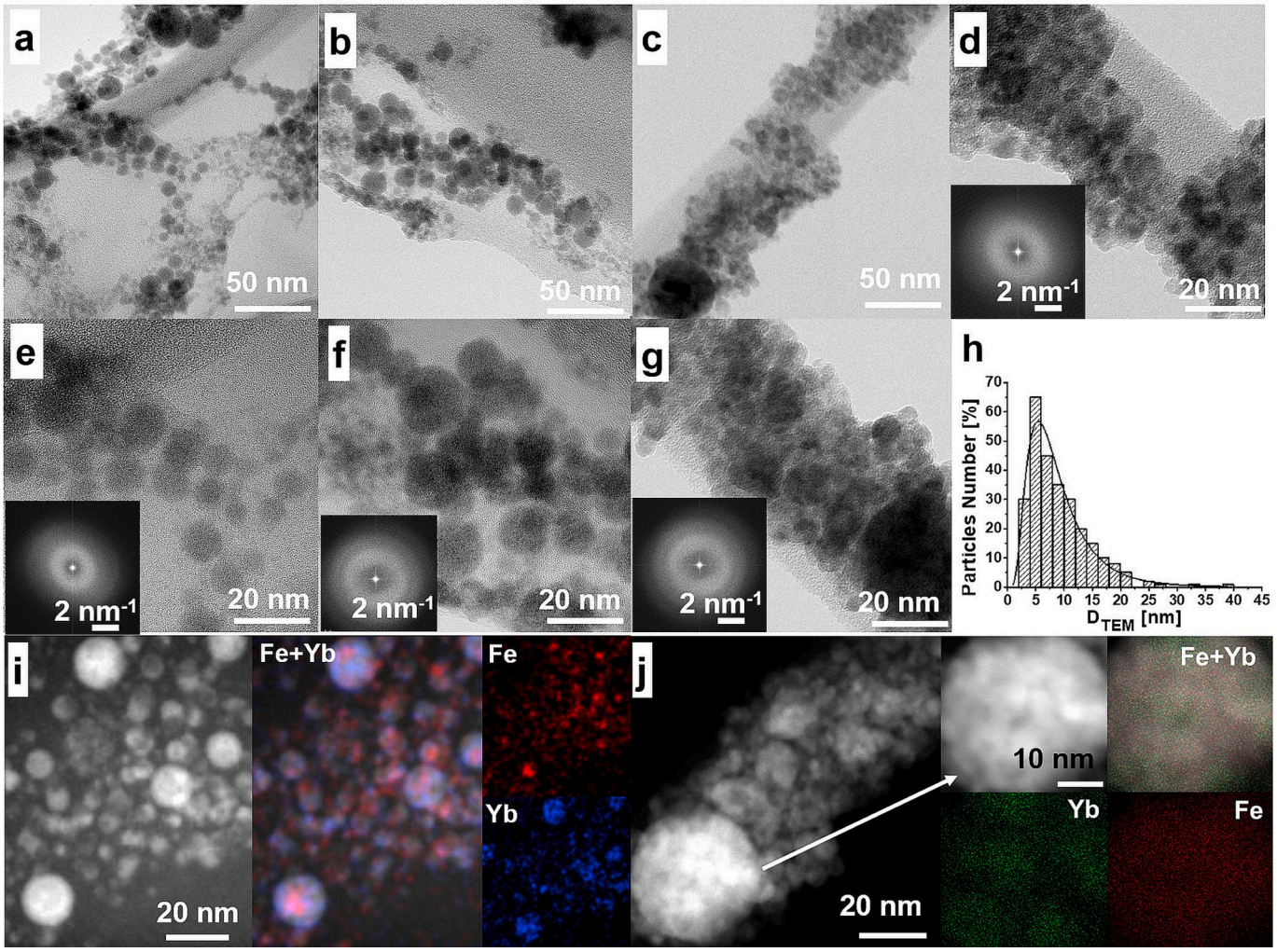

Fig. 3. Size, shape and structure and composition characterization of optimized Yb/Fe *NPs* (*O-Yb/Fe sample*). (a-c) TEM image obtained for Bright Field (BFTEM) conditions, in Diffraction Contrast mode, for O-EtOH-NPs; (d-g) HRTEM images of O-EtOH-NPs together with the calculated FFTs diagrams from the whole image regions; (h) Size distribution histogram of as synthesized O-EtOH-NPs sample; and (i-j) HAADF-STEM image and Fe and Yb EDX signals for different O-EtOH-NPs.

repetition rate from 10 kHz (Sample Yb/Fe-10, N ≈ 5) to 200 kHz (Sample Yb/Fe-13, N ≈ 96); and ii) modifying of the scanning speed from 125 $mm{\cdot}s^{-1}$ (Sample Yb/Fe-3, N ≈ 12) to 1.500 $mm{\cdot}s^{-1}$ (Sample Yb/Fe-9, N ≈ 1). In the first case, TEM and EDS analyses yielded results similar to those achieved by increasing *F* and τp (see Table 2 and Fig. 2). Thus, TEM analysis (see Supplementary Information, Figured S.I.F.3.a to S.I.F.3.d) indicated that the variation of N from 5 to 96 resulted in lognormally distributed Yb/Fe NPs populations, whose width increases progressively with *f* increasing; yielding to D_{TEM} and PDI_{TEM} values ranging from 6.6 nm to 10.9 nm and from 0.16 to 0.49, respectively. Similarly, DLS measurements of these Yb/Fe NPs transferred to DW also showed that increasing frequency produced an increase in the HD and PDI_{HD} from 118 nm to 497 nm and from 0.24 to 0.47, respectively (see Table 2 and Fig. 1). In addition, an increase in the Yb/Fe NPs concentration of the obtained colloidal dispersions from 0.0188 $mg_{NPs}{\cdot}mL^{-1}$ (ablation rate ≈ 0.39 $mg_{NPs}{\cdot}mL^{-1}{\cdot}h^{-1}$) to 0.0723 $mg_{NPs}{\cdot}mL^{-1}$ (ablation rate ≈ 1.52 $mg_{NPs}{\cdot}mL^{-1}{\cdot}h^{-1}$) was also detected. These results were in good agreement with those reported for metallic NPs [32]. On the other hand, TXRF analysis of these colloidal dispersions revealed, in all cases, Yb/Fe mass ratios between 3.2 ± 0.1.The Yb/Fe atomic ratio of these Yb/Fe NPs, which were obtained from punctual EDS analysis, increased from 0.76 to 1.1, as the NPs size increased (data not shown). Similar to previously synthesized Yb/Fe NPs in EtOH (sample Yb/Fe-3) [34], HAADF-STEM images and chemical maps (see Supplementary Information, Figured S.I.F3.e to S.I.F.3.f) demonstrated the existence of partial segregation of Yb and Fe within these NPs, even in the presence of a small population of NPs highly enriched in Yb in the samples synthesized at f values higher than 100 kHz.

The effect of the applied *N* on the characteristics of the obtained Yb/Fe NPs colloidal dispersions was confirmed through the results obtained by changing *N* from 12 to 1 by modifying the scanning speed from 125 $mm{\cdot}s^{-1}$ to 1500 $mm{\cdot}s^{-1}$ (see Table 1). Thus, TEM analysis of these Yb/Fe NPs (see Supplementary Information, Figured S.I.F.4.a) and DLS analysis of these NPs transferred to DW (see Table 2 and Fig. 2) revealed that the rise of vs values yielded to a reduction in the D_{TEM} and HD values from 7.7 nm to 6.0 nm and from 177 nm to 85 nm, respectively; whereas the PDI_{TEM} and PDI_{HD} dropped from 0.19 to 0.05 and from 0.27 to 0.21, respectively. This increase in the vs values resulted also in a diminution on the Y—Fe NPs concentration of the colloidal dispersions from 0.0240 $mg_{NPs}{\cdot}mL^{-1}$ (ablation rate ≈ 0.5 $mg_{NPs}{\cdot}mL^{-1}{\cdot}h^{-1}$) to 0.0022 $mg_{Nps}{\cdot}mL^{-1}$ (ablation rate ≈ 0.04 $mg_{NPs}{\cdot}mL^{-1}{\cdot}h^{-1}$). These results are in good agreement with those reported for metallic NPs [32]. TXRF analysis of Yb/Fe NPs samples at different scanning speeds resulted in a Yb/Fe mass ratio of 3.3 ± 0.2. On the other hand, the calculated Yb/Fe atomic ratios from punctual EDS analysis of several Yb/Fe Nps revealed an increased from 0.72 to 1.1 as the NPs size increased (data not shown). Similar to previously synthesized Yb/Fe NPs in EtOH (sample Yb/Fe-3), HAADF-STEM images and chemical maps

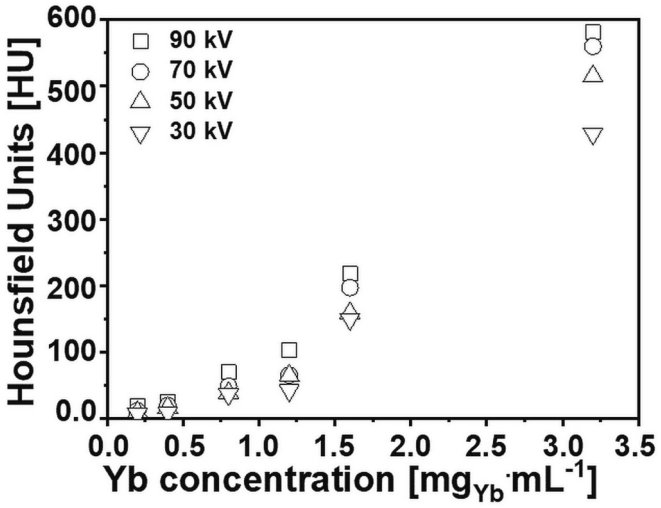

Fig. 4. Micro-CT characterization of optimized O-Yb/Fe NPs showing the CT signal intensity recorder for these NPs at X-ray tubes voltages from 30 to 90 kV plotted against the NPs concentration (from 0.2 to 3.2 mg_{NPs}•mL^{-1}).

were obtained (see Supplementary Information, fig. S.I.F.4.b and S.I.F.4. c) shows the existence of partial segregation of Yb and Fe within these NPs.

3.1.2.4. Synthesis of optimized Fe/Yb NPs. In view of the above results, it is clear which the use of low *F*, *τp*, and *N* values led to Yb/Fe NPs populations, which exhibited D_{TEM} and PDI_{TEM} smaller than 6 nm and 0.1, respectively. Once transferred to DW, these NPs yielded water-stable colloidal dispersions with HD and PDI_{HD} values lower than 140 nm and 0.21, respectively, which were within the hydrodynamic size and polydispersity values allowed for use in medical imaging techniques. Unfortunately, the use of these mild ablation conditions resulted in a strong decrease in the Yb/Fe NPs concentration in these colloidal dispersions. Therefore, the optimized generation of colloidal dispersions of Yb/Fe NPs by LA-PLA must be achieved using laser working parameters, which allows a high production of NPs (fundamentally via the use of high *F* values), coupled with those that allow a strong reduction in the HD and PDI_{HD} values (basically through the reduction of the *N* values).

Consequently, optimized colloidal dispersions of Yb/Fe NPs in EtOH (hereinafter identified as O-Yb/Fe) were synthesized using a laser pulse fluence of 8.20 J·cm^{-2} and a scanning speed of 1500 mm·s^{-1}, whereas the remaining laser working parameters reported for sample Yb/Fe-3 were used by default (see Table 1). In these conditions a stable dark toned NPs dispersion with Yb and Fe concentrations of 0.032 mg•mL^{-1} and 0.010 mg•mL^{-1} (Yb/Fe mass ratio of 3.2) were obtained; being the NPs weight collected after drying of 0.052 mg_{NPs}·mL^{-1} (ablation rate of 1.08 mg_{NPs}•mL^{-1}•h^{-1}). Once these O-Yb/Fe Nps were transferred to DW by centrifugation, a colloidal dispersion of O-Yb/Fe NPs in water was achieved, which displayed DH and PDI_{DH} values of approximately 170 nm and 0.20, respectively, meeting the requirements for the use of NPs in medical imaging. The dispersion remained stable in DW for several months at room temperature, neutral pH (7.0), and physiological pH (7.4).

TEM, HAADF-STEM, and EDS characterization of the O-Yb/Fe sample (Fig. 3) revealed that these Yb/Fe NPs presented a morphology, chemical composition, and microstructure similar to those shown by the Yb/Fe NPs synthesized in EtOH in our previous work (sample Yb/Fe-3 [34]. Thus, TEM micrographs (Fig. 3a–3c) and HAADF-STEM images (Fig. 3i and 3j) reveal the existence of well-isolated and spherical NPs (2.5 to 40 nm in size). These NPs had a lognormal size distribution (Fig. 3.h), with mean particle size (D_{TEM}) of 6.2 nm and standard deviation (SdD_{TEM}) of 2.7 nm (polydispersity index, PDI_{TEM} ~ 0.19). The HRTEM images (see Fig. 3d to 3g) did not exhibit any lattice fringes, thus NPs were determined to be non-crystalline structures. FFT from HRTEM images (which showed only the characteristic rings of the amorphous carbon coating from the Cu TEM grids, as can be observed in the insets of Fig. 3d to 3g) confirmed the low degree of crystallinity (or even amorphous structure) of these Yb/Fe NPs. HAADF-STEM images revealed the coexistence, within the same NPs, of regions with low and high image intensity, which indicates a chemical contrast in the same NP. As can be observed at the colored EDX chemical maps in Fig. 3i and 3j, such regions can be associated to Fe- and Yb rich areas of the NPs, respectively (since Yb has higher atomic mass, it is expected to yield a brighter

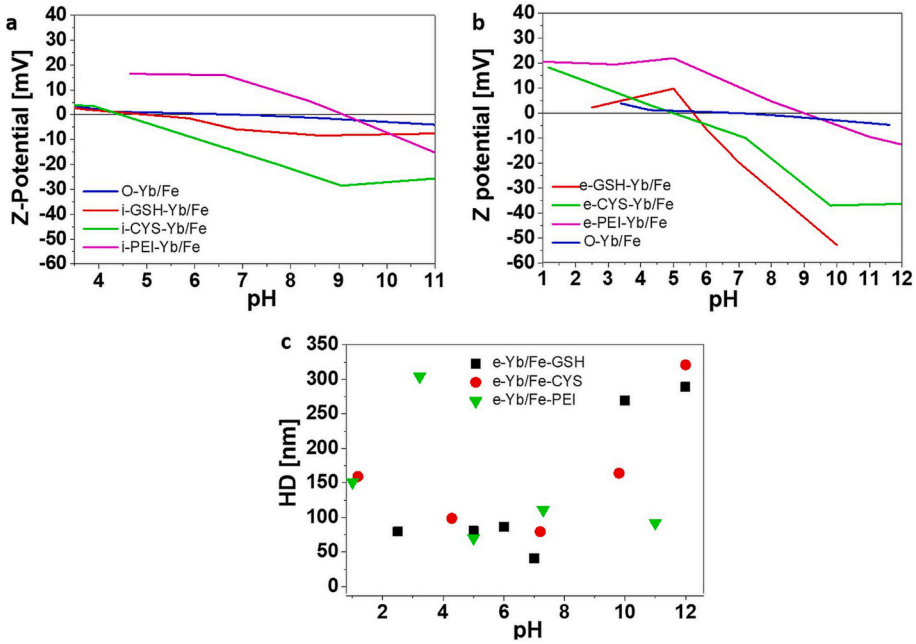

Fig. 5. Z potential as a function of pH for: (a) in situ GSH, CYS and PEI functionalized O-Yb/Fe NPs; and (b) ex situ GSH, CYS and PEI functionalized Yb/Fe NPs. (c) DLS sizes as a function of pH for ex situ functionalized NPs.

Table 3
Averaged hydrodynamic size measured by DLs for all samples.

NPs	HD (nm) DLS	PDI
O-Yb/Fe	155 ± 30	0.027
e-Yb/Fe -CYS	79 ± 27	0.381
e-Yb/Fe- GSH	40 ± 5	0.444
e-Yb/Fe-PEI	112 ± 30	0.997
i-Yb/Fe -CYS	322 ± 61	0.432
i-Yb/Fe- GSH	405 ± 45	0.444
i-Yb/Fe-PEI	853 ± 143	0.234

HAADF signal). This partial segregation of Yb and Fe was more evident for large NPs.

In addition, Fig. 4 displays the results of the micro-CT analysis of O-Yb/Fe NPs aliquots recorded at different NPs concentrations using a CT tungsten X-ray tube operating from 30 kV to 90 kV. As it can be seen, the intensity of the CT contrast signal, and therefore the X-ray attenuation ability of the O-Yb/Fe NPs, is a function of the concentration of the NPs containing the radiopaque element, in this case Yb, in the dispersions. Therefore, for all X-ray tube voltages, aliquots with O-Yb/Fe NPs concentrations lower than 1.2 $mg_{NPs} \bullet mL^{-1}$ presented CT contrast intensities in the range of those tabulated for soft tissues and substances of the human body (ranging from 0 to 60 Hounsfield units (HU)). However, above this O-Yb/Fe NPs concentration threshold, the intensity of the CT contrast increased significantly, reaching relatively high values, which were sufficient to obtain CT images with adequate contrast with respect to water and air (which are used as reference standards in CT imaging). These results demonstrate that the as-synthesized O-Yb/Fe NPs have adequate X-ray attenuation capacity for potential use as radiopaque contrast agents for the entire range of X-ray tube voltages used in medical X-ray imaging.

3.2. Functionalization and colloidal stability

The study was performed using O-Yb/Fe NPs, the optimized Yb/Fe NPs, according to the above results. Interesting alternative is to functionalize the O-Yb/Fe NPs surface by capping it with hydrophilic

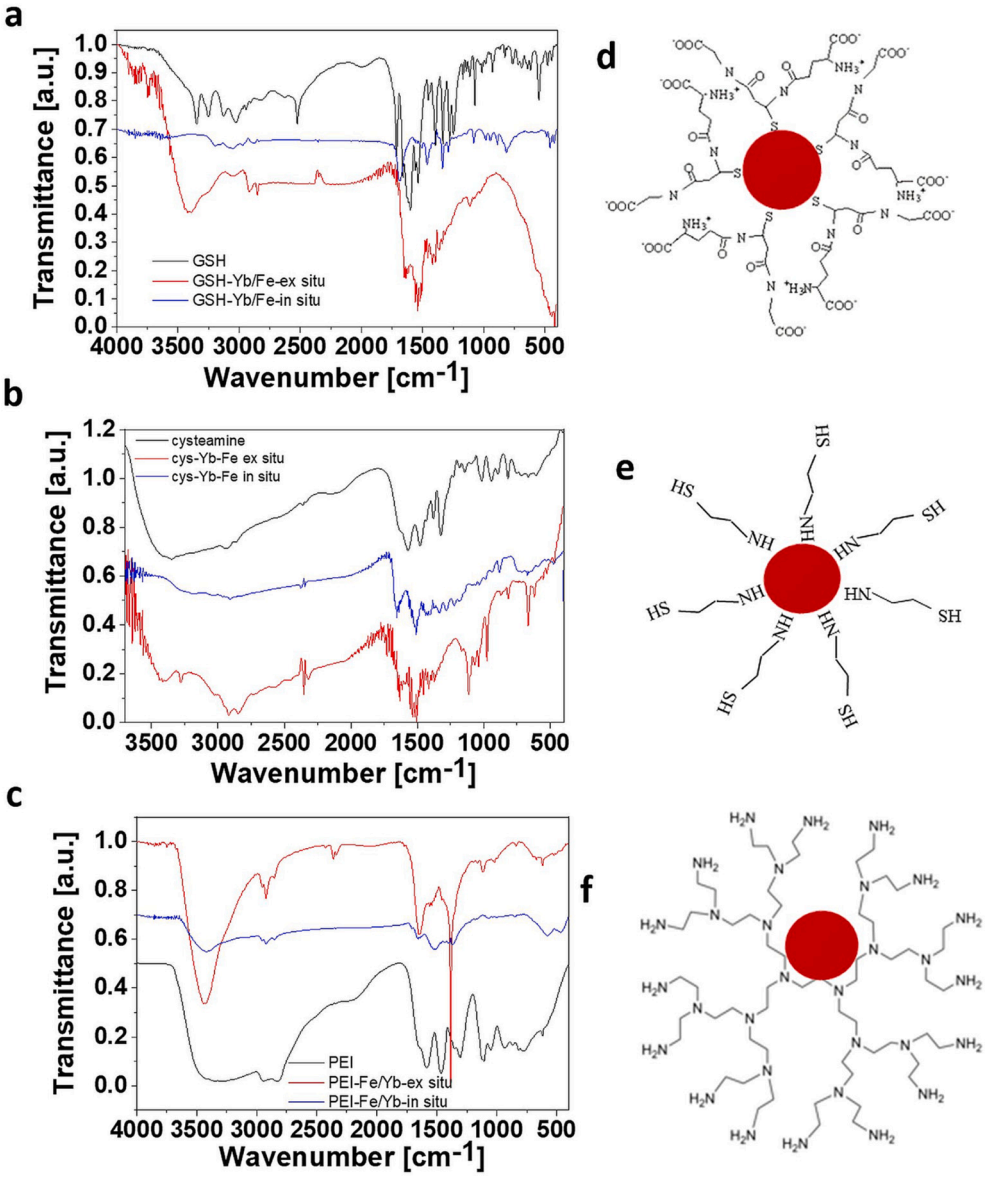

Fig. 6. (a) FTIR spectra obtained for in situ and ex situ GSH functionalized O-Yb/Fe NPs (b); in situ and ex situ CYS functionalized O-Yb/Fe NPs (c) and in situ and ex situ PEI functionalized O-Yb/Fe NPs. In all cases, the black curve represent the spectrum obtained for pure capping specie. Fig. 5d, 5e and 5f represent, respectively, schemes of the functionalized Yb/Fe NPs for GSH, CYS and PEI.

molecules containing functional groups, thereby allowing for subsequent bioconjugation. As previously described, three different compounds were chosen for the functionalization process: GSH, CYS, and PEI; and two different functionalization methods, in situ and ex situ, have been developed. Consequently, six different functionalized O-Yb/Fe NPs are obtained, which will be named by the codes: e-Yb/Fe-GSH, e-Yb/Fe-CYS and e-Yb/Fe-PEI for ex situ process and i-Yb/Fe-GSH, i-Yb/Fe-CYS and i-Yb/Fe-PEI for the in situ route.

Fig. 5 shows *Z*-potential values as a function of pH for in situ and ex situ functionalized Yb/Fe NPs (Fig. 5a and 5b respectively). As we can observe, naked O-Yb/Fe NPs present low colloidal stability, with *Z*-potential values lower than 5 mV in all the studied pH range. Figures show a general increment of Z-potential values for in situ and ex situ functionalized Yb/Fe NPs in all the pH range, indicating a general improvement of the colloidal stability when surface NP is linked to the capping agents. In the case of ex situ functionalized NPs, those capped with GSH, e-Yb/Fe-GSH NPs, presented the highest Z-potential values in the physiological pH range between pH 7 and 8. Additionally, the e-Yb/Fe-CYS NPs showed considerably high stability in this physiological pH range. In these two cases, the isoelectric point shifted to lower pH values with respect to naked Yb/Fe NPs, and the colloidal stability increased at higher pH values, with Yb/Fe NPs showing negative Z-potential values. However, the stability of the e-Yb/Fe-PEI NPs decreased from pH 5 to higher values. In this case, the isoelectric point was located at pH 9, presenting positive and lower Z-potential values in the physiological pH range. This general behavior of Yb/Fe NPs capped with PEI was also observed in the case of in situ functionalization (Fig. 5.a). However, in the case of GSH and CYS, the isoelectric points appeared at values even lower than those obtained for ex situ functionalization. The i-Yb/Fe-CYS NPs presented negative Z-potential values that were slightly higher than those obtained for e-Yb/Fe-CYS NPs. However, in the case of GSH, results point out the higher stability when ex situ mechanism is used.

Table 3 shows the hydrodynamic sizes obtained from DLS measurements at physiological pH values. A general decrease in DLS size was observed for ex situ-functionalized Yb/Fe NPs compared to naked O-Yb/Fe NPs. Comparing the three types of ex situ functionalized NPs, e-Yb/Fe-PEI is the one with higher HD value, probably due to the polymeric matrix surrounding the NP core. This behavior reveals the crucial role of the ex situ functionalization process in colloidal stabilization of NPs. The hydrodynamic size could be higher for functionalized Yb/Fe NPs owing to their capping shell; however, the decrease in NP aggregation leads to lower HD values even for Yb/Fe NPs coated with the capping molecules. This tendency is not the same for in situ functionalized Yb/Fe NPs, in which the HD values increases, probably because of the excess capping species surrounding the NP core and the possible intermediate compounds formed during ablation process. NPs size distributions obtained from these DLS experiments are shown supplementary information (see S.I.F.5).

A study of the influence of pH on the HD values of ex situ-functionalized Yb/Fe NPs was carried out. This functionalization method was chosen for this study because it leads to the formation of structures of lower HD values, and consequently, higher colloidal stability. Fig. 5.c shows the results obtained for e-Yb/Fe-GSH, e-Yb/Fe-CYS, and Yb/Fe-PEI. As we have previously remarked, e-Yb/Fe-GSH NPs show particularly low HD values at physiological pH values. The results reveal a relatively high colloidal stability for this type of Yb/Fe NPs over a broad pH range (approximately 2–10). However, higher HD values were obtained at a pH 10. In addition, a wide stability range was found in the case of e-Yb/Fe-CYS with HD values lower than 100 nm at physiological pH and below 175 nm until pH 10. For higher pH values, the tendency was similar to that of e-Yb/Fe-GSH. Although e-Yb/Fe-GSH are NPs with lower HD values at physiological pH values, e-Yb/Fe-CYS are NPs with the broadest range of stability (sizes lower than 200 nm). In the case of e-Yb/Fe-PEI the HD values are higher at lower pH, however, Yb/Fe NPs present relatively low HD values at physiological pH range and even at pH higher than 10, range in which the functionalization with GSH or CYS promotes less stability. This behavior, which clearly depends on the free functional groups in the capping molecules, is of crucial importance for subsequent conjugation.

3.3. Functionalization mechanisms (FT-IR)

In order to deepen in the functionalization processes, Fourier Transform Infrared Spectroscopy (FTIR) spectra of ex situ and in situ Yb/Fe-GSH (a), Yb/Fe-CYS (b) and Yb/Fe-PEI (c) NPs, as well as the corresponding pure capping ligands are shown in Fig. 6. The FT-IR spectra of functionalized NPs, in comparison to those corresponding to pure ligands, allowed us to probe the binding between NP and ligands.

In all cases, the red curves represent the ex situ functionalized Yb/Fe NPs, blue curves correspond to the in situ functionalized Yb/Fe NPs, and the black curves represent the free capping species used in each case. In general, all functionalized Yb/Fe NPs spectra showed a band around 3425 cm^{-1}, attributed to the OH vibration due to adsorbed water. Spectra corresponding to in situ functionalized Yb/Fe NPs show, in general, much more similarity with the corresponding pure capping species. This could be due to an excess of capping surrounding the Yb/Fe NPs cores induced by the in situ functionalization process.

For Yb/Fe NPs functionalized with GSH (Fig. 6.a), the free GSH spectrum shows a peak at 3350 cm^{-1}, characteristic of the -NH_2 group, a peak at 2530 cm^{-1} due to the S—H stretching group, and a peak at 1600 cm^{-1}, which is representative of -COOH stretching [20]. The peak at 2530 cm^{-1} that, as we have indicated, corresponds to the S—H stretching vibration of GSH, is disappeared in both, ex situ and in situ GSH-Yb/Fe NPs, which indicates that the GSH molecules anchor on the surface of NPs through —S bonding, instead of using the amino or carboxylic groups.

However, this capping mechanism, although the thiol group, does not seem to be the majority in the case of Yb/Fe NPs functionalized with CYS. Fig. 6.b shows the FTIR spectra for ex situ and in situ Yb/Fe-CYS NPs and pure CYS. In this case, the peak of the S—H stretching vibration located around 2531 cm^{-1} in the pure CYS spectrum, also appears for e-Yb/Fe-CYS, indicating that, majority, cysteamine does not attach to the Yb/Fe NPs via the thiol group Additionally, the spectrum corresponding to pure CYS displayed two bands at 3233 cm^{-1} and 1560 cm^{-1}, corresponding to the N—H vibration from amine groups, as well as the one from the C—N vibration at 1316 cm^{-1} [67]. The lack of this last peak in the spectra obtained from Yb/Fe-CYS, especially in the case of ex-situ functionalization, together with the intensity decrease in the band at 3233 cm^{-1}, could indicate that cysteamine is linked to the Yb/Fe NPs surface through the amine group. The C—H asymmetric stretching band, between 2930 and 2840 cm^{-1}, can be more clearly appreciated for both ex situ and in situ Yb/Fe-CYS NPs than for pure CYS, owing to the decrease in the intensity of the 3233 cm^{-1} N-H vibration band.

Finally, the FT-IR spectra for pure PEI and ex situ and in situ Yb/Fe-PEI are shown in Fig. 6.c. The primary alkylamine (C—N) and aminomethyl ($-NH_2$) groups in the PEI structure were identified by their unique peaks. Peaks were observed at 1580–1640 cm^{-1} (NH_2 scissoring) and 3250–3400 cm^{-1} (NH_2 stretching). In addition, amino methyl ($H_2C–CH_2NH_2$) groups were identified based on the peaks (CH_2 scissoring; 2830–2885 cm^{-1}) [68]. The spectra of Yb/Fe-PEI showed a considerable decrease in the intensities of these characteristic bands. Although spectra from Yb/Fe NPs and the reference show a similar profile, the highest difference is located in the range between 1580 and 1640 cm^{-1} (-NH_2 scissoring), revealing a possible linking mechanism through amino groups for both cases, in situ and ex situ functionalization.

These results reveal that the functionalizing species surround the Yb/Fe NPs surface. In the case of PEI, the molecules likely surround the Yb/Fe NPs surface via electrostatic interactions. In the case of GSH, the thiol group links the Yb/Fe NPs surface by S bonding, whereas the cysteamine molecule seems to use its amine terminal group to attach to the Yb/Fe NPs cores. Fig. 6d, 6e and 6f shows a scheme of the Yb/Fe NPs cores

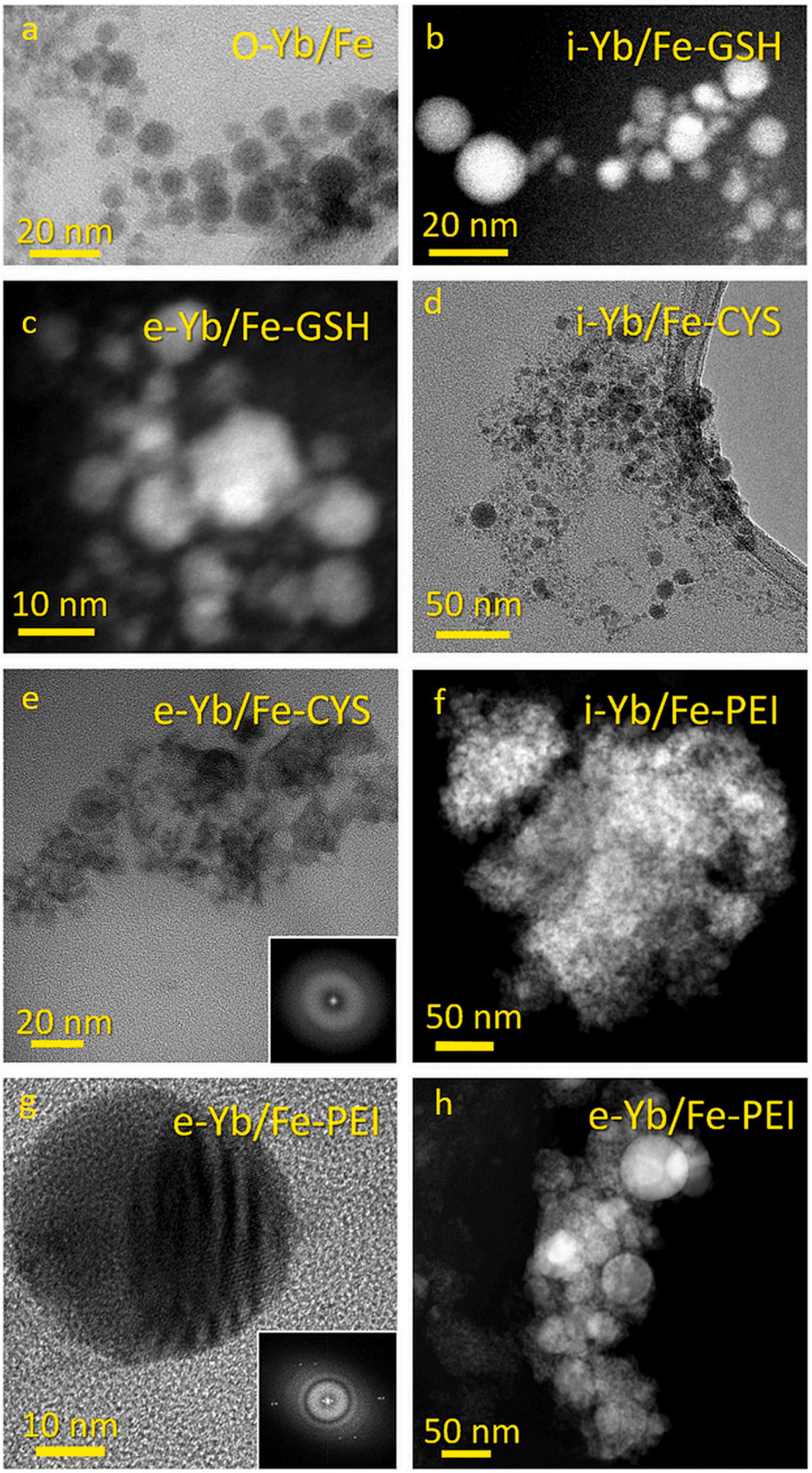

Fig. 7. BFTEM, HRTEM and STEM-HAADF micrographs for: (a) non-functionalized O-Yb/Fe NPs; (b) i-Yb/Fe-GSH; (c) e-Yb/Fe-GSH; (d) i-Yb/Fe-CYS; (e) e-Yb/Fe-CYS; (f) i-Yb/Fe-PEI,; and (g-h) e-Yb/Fe-PEI.

Table 4
Averaged D_{TEM} Yb/Fe NPs measured by TEM for all samples.

Sample	Size (nm)
e-Yb/Fe-GSH	7 ± 4
i-Yb/Fe-GSH	10 ± 6
e-Yb/Fe-CYS	10 ± 5
i-Yb/Fe-CYS	7 ± 3
e-Yb/Fe-PEI	10 ± 4
i-Yb/Fe-PEI	12 ± 5

linked to the capping shell, evidencing the proposed linkage mechanism for GSH, CYS, and PEI.

No evidences of differences in the linkage mechanisms between ex situ and in situ functionalization processes are observed. However, in situ functionalized Yb/Fe NPs spectra show, in general, profiles more similar to those corresponding to the pure capping. This can be attributed to an excess of ligand molecules in the case of in-situ functionalization synthesis, in which the capping agent is introduced into the liquid used in the laser ablation process.

3.4. Functionalization effects on structural properties

TEM measurements were performed to study the possible influence of the functionalization process on the size distribution and morphology of Yb/Fe NPs. Fig. 7 shows an image of the non-functionalized O-Yb/Fe NPs (Fig. 7. a) for comparison, and representative micrographs of i-Yb/Fe-GSH (Fig. 7. b), e-Yb/Fe-GSH (Fig. 7.c), and i-Yb/Fe-CYS (Fig. 7. d), and e-Yb/Fe-CYS (Fig. 7. e), and i-Yb/Fe-PEI (Fig. 7. f) and e-Yb/Fe-PEI (Fig. 7.h). These images were obtained using bright-field TEM (BFTEM) conditions for Diffraction Contrast; HRTEM; and HAADF-STEM modes. Fig. 7.g presents an HRTEM image of an e-Yb/Fe-PEI NP, in which the NP core structure is observed, revealing a partially crystalline nature. The average Yb/Fe NP sizes (DTEM) obtained using >100 NPs are listed in Table 4. NPs size distribution obtained by TEM are shown in supplementary information (see F.I.F.6).

The formation of homogeneous, well-distributed, and spherical Yb/Fe NPs was observed in all the cases. In particular, small sizes were found in the case of i-Yb/Fe-PEI NPs, where small NPs were enweaved in an amorphous matrix, probably owing to the effect of the excess polymer.

TEM and STEM results revealed that the functionalization procedure (in situ or ex situ) had no significant influence on the dispersion or size of the Yb/Fe NPs, nor did it result in a different degree of adherence of the capping agent to the Yb/Fe NPs cores.

3.5. Chemical composition and functionalization efficiency

The EDX point spectra were used to study the chemical composition of the Yb/Fe NPs. Fig. 8 shows examples of these spectra for non-functionalized Yb/Fe NPs, as well as for each in situ and ex situ functionalized Yb/Fe NPs. The peak heights were normalized to those corresponding to the X-ray emissions due to the de-excitation of the M energy level for Yb atoms (which are indicated in each spectrum in the figure). Yb and Fe signals were detected in all cases, indicating the existence of both elements in the NP. For e-Yb/Fe-GSH, i-Yb/Fe-GSH, e-Yb/Fe-CYS, and i-Yb/Fe-CYS, a sulfur peak appeared because of the presence of sulfur in the compounds used for the functionalization of these Yb/Fe NPs (glutathione or cysteine). As can be observed, the S-peaks present comparable intensities (and thus, proportions of Yb) for both in situ and ex situ functionalization, revealing that the Yb/Fe NPs were coated by the capping agent in all cases. Because the PEI polymer is formed only by low-atomic-mass elements, EDX cannot accurately identify the functionalization in the e-Yb/Fe-PEI and i-Yb/Fe-PEI samples, and only Fe and Yb signals were obtained as components for NPs in these cases. The peaks that can be associated with C, O, and N (although not labeled in the spectra, all correspond to the peaks at lower energies than those of the Yb-M peak) and Cu are explained by the carbon support and the copper mesh utilized in the TEM grids and by the components of the different species utilized for functionalization. The S-peak constitutes an interesting corroboration of the proper functionalization of GSH and CYS for both in situ and ex situ methods.

Fig. 9 summarizes the most remarkable results of Yb/Fe NPs chemical characterization of the Yb/Fe NPs via EDX map spectroscopy. This figure presents the HAADF images and EDX maps from the areas of different samples. Both techniques allow qualitative inspection of the compositional homogeneity of Yb/Fe NPs. As previously found for the naked optimized Fe/Yb NPs, these compositional maps also show

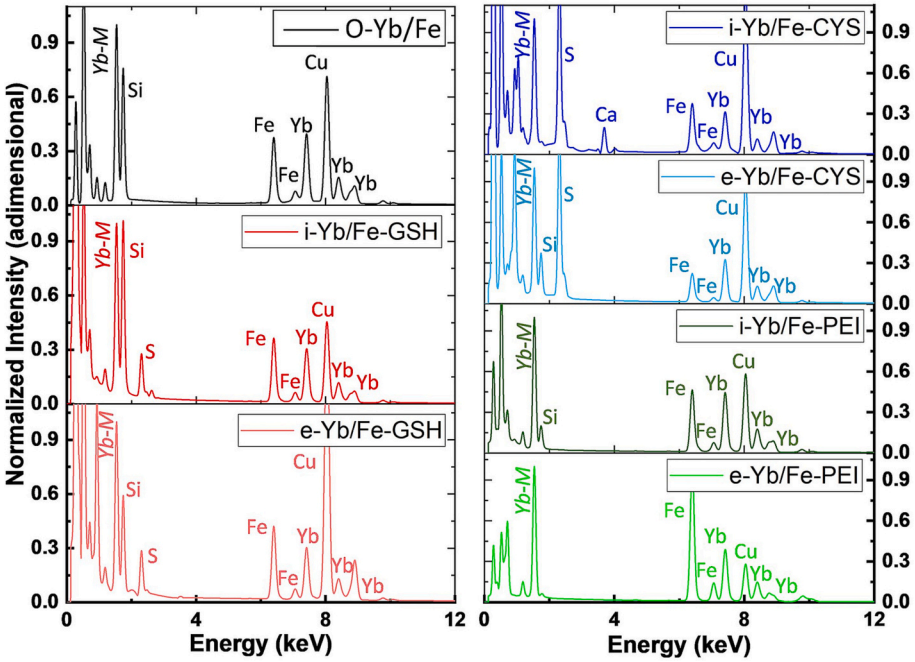

Fig. 8. Normalized EDX point spectra for ex situ and in situ functionalized O-Yb/Fe NPs.

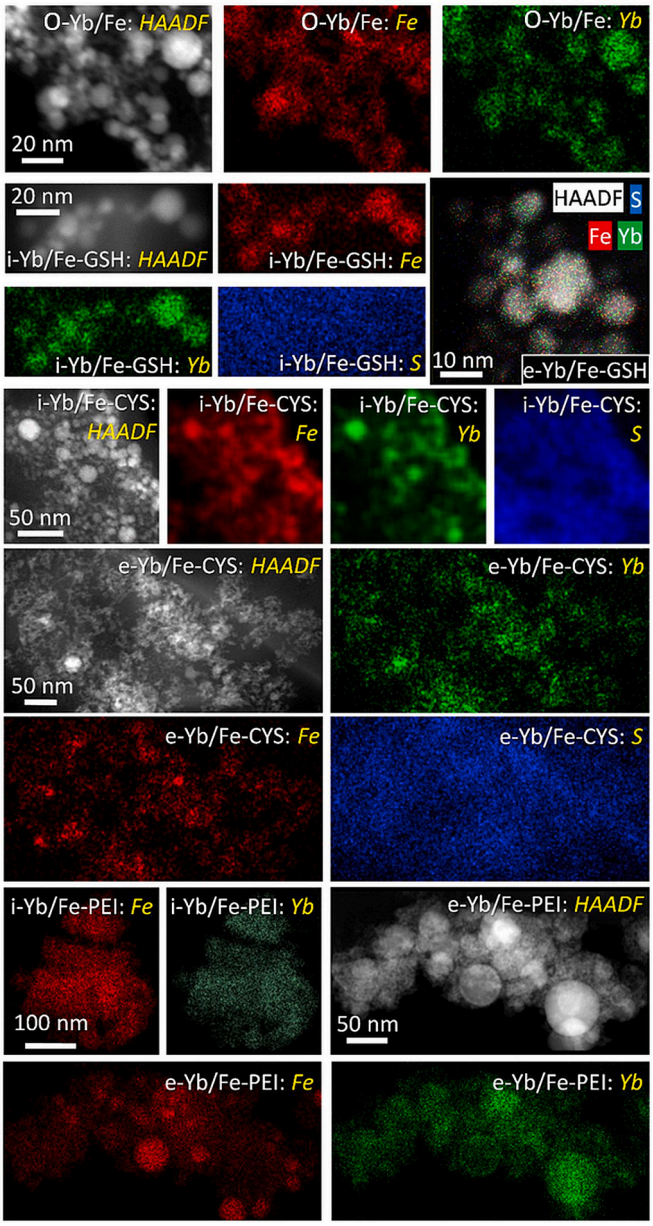

Fig. 9. EDX maps for naked O-Yb/Fe NPs as well as all the in situ and ex situ functionalized Yb/Fe NPs.

homogeneous distributions of Yb and Fe atoms in the functionalized Yb/Fe NPs. In the case of Yb/Fe-GSH and Yb/Fe-CYS, as we have previously explained, this technique not only provides information about Yb and Fe distribution but also allows verification of the functionalization process by studying the sulfur map derived from GSH (b) or cysteamine (c). It can be observed that the Fe and Yb signals corresponding to functionalized Yb/Fe NPs, are in good agreement with the HAADF images of the Yb/Fe NPs, as previously reported for naked Yb/Fe NPs. In the samples with S-containing functionalization molecules (e-Yb/Fe-GSH, i-Yb/Fe-GSH, e-Yb/Fe-CYS, and i-Yb/Fe-CYS), sulfur signals were detected covering the Yb/Fe NPs cores. However, in situ cysteamine- and glutathione-functionalized Yb/Fe NPs show some sulfur signals in the space between Yb/Fe NPs, probably due to an excess of sulfur caused by the in situ synthesis process, in which the capping agent is introduced into the liquid used for the laser ablation process. This excess of functionalizing species in the cases of in-situ synthesis is in good agreement with the results obtained from FT-IR spectroscopy. As mentioned above, in the case of e-Yb/Fe-PEI and i-Yb/Fe-PEI, the capping molecules were composed of carbon, oxygen, nitrogen, and hydrogen. Signals from these light elements were not detected by this technique. The signals corresponding to the carbons of the capping molecules were screened by those corresponding to the carbon support and residual organic particles possibly present in the electron microscopy grid.

Therefore, it can be concluded that, homogeneous and appropriately functionalized Yb/Fe NPs were obtained. Although both in situ and ex situ functionalization methods led to capped Yb/Fe NPs, an excess of capping agent was detected in the case of the in situ process.

3.6. Biocompatibility and medical image potential applications

3.6.1. Cytotoxicity

As previously indicated, one key property of these Yb/Fe NPs in medical applications is their cytotoxicity, which can be initially studied through cytotoxicity assays. Cytotoxicity measurements were performed to determine whether the capping shell induced a decrease in the toxicity of O-Yb/Fe NPs compared to those without functionalization. MTT assays were performed to evaluate the viability of Jurkat T cells cultured in the presence or absence of different Yb/Fe NPs (Fig. 10). The graphs show the mean (bars) and standard deviation of three independent experiments performed in triplicate, corresponding to the percentage of viable cells cultured in the presence of naked and in situ functionalized O-Yb/Fe NPs (Fig. 10. a), and ex situ-functionalized O-Yb/Fe NPs (Fig. 10. b) at a concentration of 1.5 μgNPs•mL-1, considering the viability of cultured cells not exposed to NPs as 100%.

Although cell viability remained over 80% in the case of the in situ-functionalized O-Yb/Fe NPs (Fig. 10. a), we must consider that naked O-Yb/Fe NPs do not show cytotoxicity even at higher concentrations. The loss of cell viability in the case of in situ functionalized NPs was due to the functionalization process. In contrast, no significant cytotoxicity was observed when ex situ-functionalized O-Yb/Fe NPs were used (Fig. 10b and 10c). The cell viability reached values near 100% in all cases for the ex situ process. Viability percentages higher than 100, can be explained by the fact that lysosomal degradation of some nanomaterials, such as iron, can result in a source of cell nutrients, favoring cell survival and proliferation. Thus, the high level of viability of Jurkat T cells incubated with e-Yb/Fe NPs could be explained by these processes. To determine cell viability using ex situ-functionalized O-Yb/Fe NPs, the NPs concentration was increased to 15 μg NPs •mL-1 (Fig. 10.c). Even at this relatively high Yb/Fe NPs concentration, the experiment revealed a low cytotoxicity for all ex situ-functionalized O-Yb/Fe NPs, retaining cell viability at values near 100%, with the exception of e-Yb/Fe-PEI NPs at higher concentrations. In particular, good biocompatibility was obtained for e-Yb/Fe-GSH NPs. The GSH molecules seems to properly surround the Yb/Fe cores, increasing the Yb/Fe NPs biocompatibility

3.6.2. Medical image potential applications

e-Yb-Fe-GSH NPs have been chosen for medical image measurements due to their suitable colloidal and biocompatible properties. CT and MRI images at different phantom concentrations were studied, and the results obtained from these experiments are shown in Fig. 11. The CT images obtained at different e-Yb-Fe-GSH NPs concentrations are shown in Fig. 11. a, and the corresponding X-ray attenuation (CT) intensity values as a function of the concentration are shown in Fig. 11.b. As expected, the CT signal of these functionalized Yb/Fe NPs increased with Yb concentration, reaching relatively high values at a concentration of 3.1 mgNPs •mL-1. For e-Yb-Fe-GSH NPs concentrations lower than 1.5 mgNPs•mL-1, there was no significant increase in CT contrast; however, the signal intensity increased considerably for higher -Yb-Fe-GSH NPs concentrations (Liang, Zhou et al. 2015), in accordance with the results obtained from the micro-CT characterization of the nude O-Yb/Fe NPs.

We also evaluated the contrast capability of the e-Yb/Fe-GSH NPs for T2 weighted MRI, at different Fe concentrations. (Liang, Zhou et al. 2015) Fig. 11.c shows the T2 modal MRI for the e-Yb/Fe-GSH NPs at different concentrations. The T2 signals indicate the potential of these e-

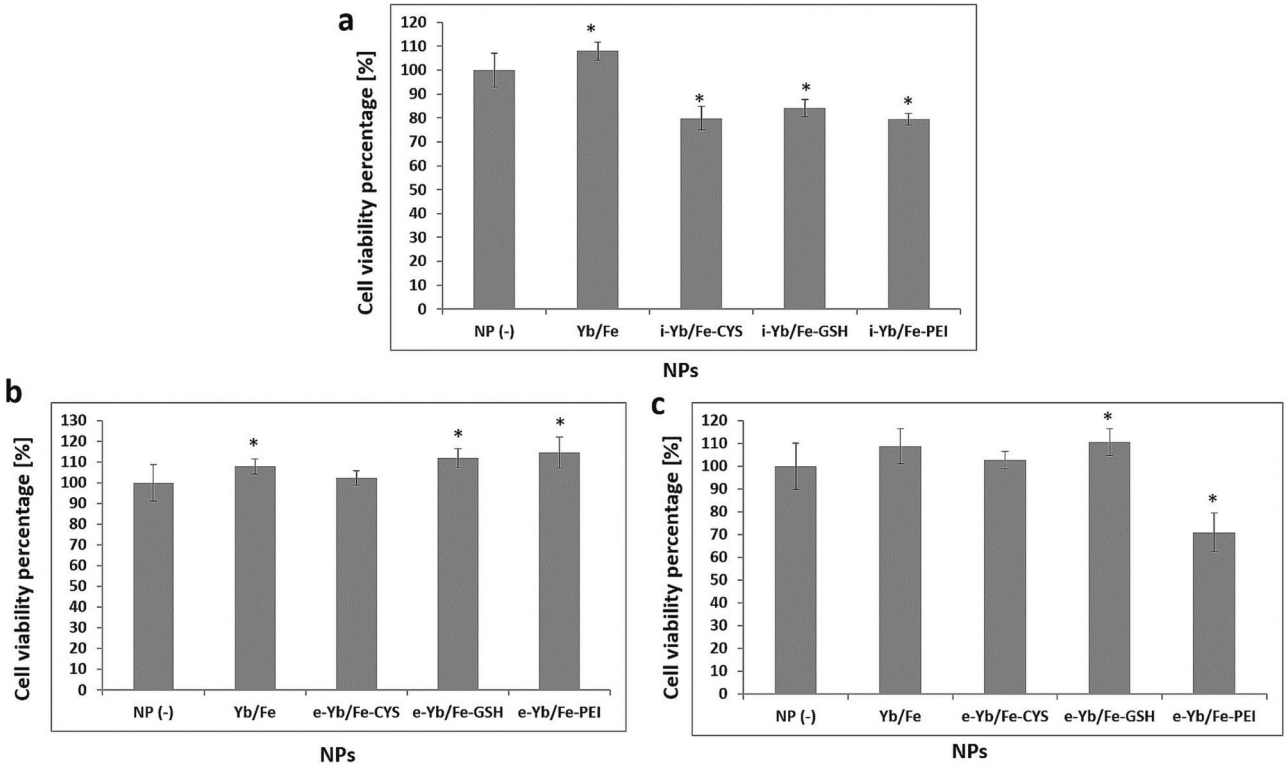

Fig. 10. MTT Cell Viability assay of Jurkat T cells incubated with the indicated type of NPs: (a) for in situ functionalization in the presence of Yb/Fe NP concentrations of 1.5 μg/mL; (b) for ex situ functionalization in the presence of Yb/Fe NPs concentrations of 1.5 μg/mL; and (c) for ex situ functionalization in the presence of Yb/Fe NPs concentrations of 15 μg_{NPs}/mL. In all cases the NPs (−) represent the cultured cells not exposed to NPs. Bar graphs represent the distribution of the mean and standard deviation of three independent experiments performed in triplicate. The percentage of viable cells from Jurkat T cells cultured in the absence of NPs was considered as 100%. Statistically significant differences between each sample and the control sample (NP (−)) ($p < 0.05$) are marked with an asterisk (*). Statistical analysis was performed using the Statgraphics software. Significance was determined using and ANOVA, Multiple Range Test and Student's *t*-test. Mean of viability data obtained for cells cultured in the presence of 10% dimethyl sulfoxide (DMSO) was 8.79%.

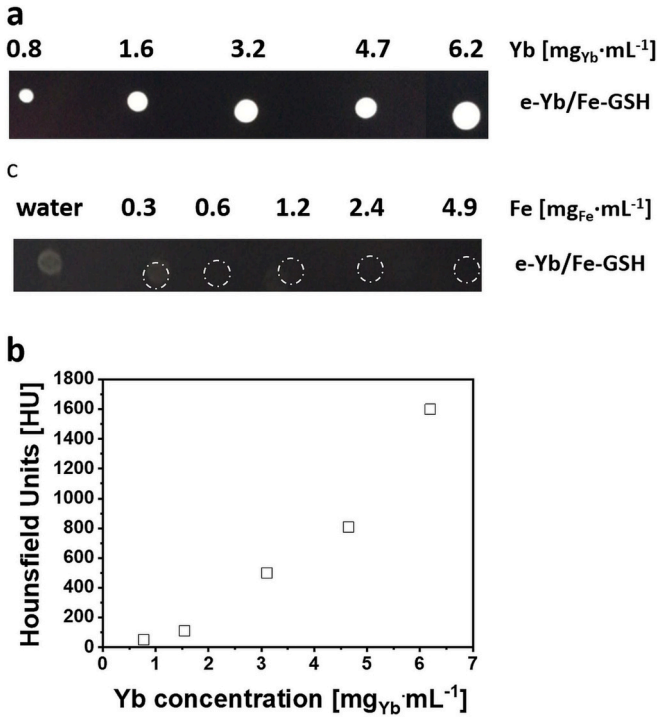

Fig. 11. (a) CT images of e-Yb/Fe-GSH NPs at different concentrations. (b) CT signal intensity of e-Yb/Fe-GSH NPs plotted against the concentration. (c) The T2 -weighted MR images of e-Yb/Fe-GSH NPs at different concentrations.

Yb-Fe-GSH NPs as powerful negative T2 MRI contrast agents. The signal enhancement significantly increased even at the lowest Yb/Fe NPs concentration, indicating the potential of e-Yb/Fe-GSH as a powerful negative T2 contrast agent (Wang, Gao et al. 2016) (Yeste, Fernandez-Ponce et al. 2022).

4. Conclusions

Optimization experiments revealed that using low fluence values and low pulse accumulation per spot values, resulted in the production of water stable colloidal dispersions of O-Yb/Fe NPs with hydrodynamic size and polydispersity <90 nm and 0.21 (DTEM and PDITEM <6.0 and 0.06, respectively). The use of these parameters, however, resulted in a significant decrease in the NPs concentration of these colloidal dispersions. As a result, a balance between low pulse accumulation per spot value and high fluence values must be used to produce sufficient quantities of optimized Yb/Fe with appropriate hydrodynamic size and polydispersity for their potential use in medicine.

In situ and ex situ functionalization of the optimized O-Yb/Fe NPs, using GSH, CYS, and PEI as capping agents, has been successfully implemented, increasing the colloidal stability of naked-synthetized O-Yb/Fe NPs in all cases. The resulting functionalized O-Yb/Fe NPs exhibited relatively high *Z*-potentials at physiological pH. Different linking mechanisms were found depending on the capping species but not on the functionalization route (in situ or ex situ).

In all cases, the optimized and functionalized O-Yb/Fe oxide NPs exhibited a homogeneous distribution of Yb and Fe atoms inside the NPs. Although both in situ and ex situ functionalization methods provide proper coverage of O-Yb/Fe NPs in which the capping agent surrounds the NPs surface, excess capping and intermediate species formed during

ablation process in the case of in situ process causes an important increase in the hydrodynamic diameter and consequent loss of colloidal stability.

Although all functionalized O-Yb/Fe NPs exhibited appropriate biocompatibility, the results revealed a loss in cell viability when in situ functionalized NPs were used, probably because of the toxicity promoted by the products originating during the in situ process. Excess capping can also harm subsequent bioconjugation with other biological species in the case of NPs obtained via the in situ route. The high biocompatibility and low cytotoxicity of the e-Yb/Fe-GSH NPs, together with their colloidal stability and suitable superficial characteristics for subsequent bioconjugation, suggest the potential of these functionalized NPs in biomedical applications. Additionally, e-Yb/Fe-GSH NPs showed good CT imaging ability and elevated negative T2 contrast, even at low Yb/Fe NPs concentrations, thereby indicating their promising potential as dual MRI/CT contrast agents.

In summary, we designed and optimized a novel method for manufacturing nanoparticles with high stability and biocompatibility by liquid laser ablation, surrounded by a species that allows subsequent binding to biomolecules. Although ex situ functionalized nanoparticles with GSH gave the best results, we present other possibilities that may be of vital interest depending on the subsequent unions pursued.

Declaration of Competing Interest

The authors declare no conflict of interest.

Data availability

Data will be made available on request.

Acknowledgment

This research has been funded by the Spanish Ministry of Economy and Competitiveness (MINECO) and FEDER [research projects MAT2015-67354R], the H2020 Action H2020-MSCA-IF-2014_ST [grant 656908-NIMBLIS] of the Executive Agency for Research Manages of EU Commission, the Proyectos Integradores MdM-IMEYMAT 2020 call (research project ULST-NANO), and the projects PECART-0096-2020 (Consejería Salud y Familias. JA Spain) and P20_01293 (Consejería Economía, Conocimiento, Empresas y Universidad. JA Spain). In addition, we acknowledge the received technical assistance from the SC-ICYT of the University of Cádiz. We also acknowledge to the Networking Research Centre on Bioengineering, Biomaterials, and Nanomedicine (CIBERBBN) (which is financed by the Instituto de Salud Carlos III (ISCIII) with assistance from the European Regional Development Fund (ERDF)) and the ICTS "NANBIOSIS", specifically the FVPR/U20 (http://www.nanbiosis.es/portfolio/u20-in-vivo-experimentalplatform/) for providing access to the micro-CT. M.L. was supported by a post-doctoral grant of the Consejo Nacional de Ciencia y Tecnología from Mexico (CONACYT, no 619639). Finally, we want to thank the company LASING S.L. its technical support in the development of the NANO-GLAS laser system where the LA-PLA experiments were carried out.

Appendix A. Supplementary data

Supplementary data to this article can be found online at https://doi.org/10.1016/j.powtec.2023.118733.

References

[1] T. Nguyen Thi Kim, Functional nanoparticles for biomedical applications, Nanoscale 5 (2013) 11338.
[2] A.U. Khan, L. Chen, G. Ge, Recent development for biomedical applications of magnetic nanoparticles, Inorg. Chem. Commun. 134 (2021).
[3] G. Bao, S. Mitragotri, S. Tong, Multifunctional nanoparticles for drug delivery and molecular imaging, in: M.L. Yarmush (Ed.), Annual Review of Biomedical Engineering vol 152013, 2023, pp. 253–282.
[4] S. Sharma, N. Lamichhane, T. Parul, I. Roy Sen, Iron oxide nanoparticles conjugated with organic optical probes for in vivo diagnostic and therapeutic applications, Nanomedicine 16 (2021) 943–962.
[5] A. Khalid, R. Norello, A.N. Abraham, J.-P. Tetienne, T.J. Karle, E.W.C. Lui, K. Xia, P.A. Tran, A.J. O'Connor, B.G. Mann, R. de Boer, Y. He, A.M.C. Ng, A.B. Djurisic, R. Shukla, S. Tomljenovic-Hanic, Biocompatible and biodegradable magnesium oxide nanoparticles with in vitro photostable near-infrared emission: short-term fluorescent markers, Nanomaterials 9 (2019).
[6] C. Xia, X. Jin, H.A.L. Garalleh, M. Garaleh, Y. Wu, J.M. Hill, A. Pugazhendhi, Optimistic and possible contribution of nanomaterial on biomedical applications: a review, Environ. Res. 218 (2023).
[7] Y. Zhao, W. Song, J. Xu, T. Wu, Z. Gong, Y. Li, B. Li, Y. Zhang, Light-driven upconversion fluorescence micromotors, Biosens. Bioelectron. 221 (2023).
[8] Y. Li, M. Wang, Y. Tao, R. Zhang, M. Zhou, P. Tao, P. Feng, W. Huang, H. Huang, W. Miao, Highly stable and biocompatible nanocontrast agent encapsulating a novel organic fluorescent dye for enhanced cellular imaging, Powder Technol. 358 (2019) 110–119.
[9] T.-A. Le, M.P. Bui, J. Yoon, Development of small-rabbit-scale three-dimensional magnetic particle imaging system with amplitude-modulation-based reconstruction, IEEE Trans. Ind. Electron. 70 (2023) 3167–3177.
[10] S.K. Nune, P. Gunda, P.K. Thallapally, Y.-Y. Lin, M.L. Forrest, C.J. Berkland, Nanoparticles for biomedical imaging, Expert Opin. Drug Deliv. 6 (2009) 1175–1194.
[11] S. Kenouche, J. Larionova, N. Bezzi, Y. Guari, N. Bertin, M. Zanca, L. Lartigue, M. Cieslak, C. Godin, G. Morrot, C. Goze-Bac, NMR investigation of functionalized magnetic nanoparticles Fe3O4 as T-1-T-2 contrast agents, Powder Technol. 255 (2014) 60–65.
[12] G. Hashimoto, M. Fukui, P. Sorajja, J.L. Cavalcante, Essential roles for CT and MRI in timing of therapy in tricuspid regurgitation, Prog. Cardiovasc. Dis. 62 (2020) 459–462.
[13] N. MacRitchie, M. Frleta-Gilchrist, A. Sugiyama, T. Lawton, I.B. McInnes, P. Maffia, Molecular imaging of inflammation - current and emerging technologies for diagnosis and treatment, Pharmacol. Ther. 211 (2020).
[14] R. Fusco, N. Raiano, C. Raiano, F. Maio, P. Vallone, M.M. Raso, S.V. Setola, V. Granata, M.R. Rubulotta, M.L. Barretta, T. Petrosino, A. Petrillo, Evaluation of average glandular dose and investigation of the relationship with compressed breast thickness in dual energy contrast enhanced digital mammography and digital breast tomosynthesis, Eur. J. Radiol. 126 (2020).
[15] S.H. Heywang-Koebrunner, A. Hacker, S. Sedlacek, Magnetic resonance imaging: the evolution of breast imaging, Breast 22 (2013) S77–S82.
[16] L.M. Canter, Anaphylactoid reactions to radiocontrast media, Allergy Asthma Proc. 26 (2005) 199–203.
[17] A. Lahooti, S. Sarkar, S. Laurent, S. Shanehsazzadeh, Dual nano-sized contrast agents in PET/MRI: a systematic review, Contrast Media Mol. Imaging 11 (2016) 428–447.
[18] E. Forte, D. Fiorenza, E. Torino, A.C. di Polidoro, C. Cavaliere, P.A. Netti, M. Salvatore, M. Aiello, Radiolabeled PET/MRI nanoparticles for tumor imaging, J. Clin. Med. 9 (2020).
[19] R. Meenambal, S. Kannan, Cosubstitution of lanthanides (Gd3+/Dy3+/Yb3+) in beta-Ca-3(PO4)(2) for upconversion luminescence, CT/MRI multimodal imaging, Acs Biomater. Sci. Eng. 4 (2018) 47–56.
[20] M.P. Yeste, C. Fernandez-Ponce, E. Felix, M. Tinoco, R. Fernandez-Cisnal, C. Garcia-Villar, C. Pfaff, J. Kriwet, E. Natividad, M.A. Cauqui, F. Garcia-Cozar, R. Litran, O. Bomati-Miguel, Solvothermal synthesis and characterization of ytterbium/iron mixed oxide nanoparticles with potential functionalities for applications as multiplatform contrast agent in medical image techniques, Ceram. Int. 48 (2022) 31191–31202.
[21] K. Kaliyamoorthy, A.S. Pillai, A. Alexander, A. Arivarasu, I.V.M.V. Enoch, S. Ramasamy, beta-Cyclodextrin-folate functionalized poly(lactic-co-glycolide)-superparamagnetic ytterbium ferrite hybrid nanocarrier for targeted delivery of camptothecin, Mater. Sci. Eng. C-Mater. Biol. Appl. 122 (2021).
[22] X. Shi, C. Wang, Y. Ma, H. Liu, S. Wu, Q. Shao, Z. He, L. Guo, T. Ding, Z. Guo, Template-free microwave-assisted synthesis of FeTi coordination complex yolk-shell microspheres for superior catalytic removal of arsenic and chemical degradation of methylene blue from polluted water, Powder Technol. 356 (2019) 726–734.
[23] H. Kobayashi, K. Fujiwara, N. Kobayashi, T. Ogawa, M. Sakai, M. Tsujimoto, O. Seri, S. Mori, N. Ikeda, Stability of cluster glass state in nano order sized YbFe2O4 powders, J. Phys. Chem. Solids 103 (2017) 103–108.
[24] J. Zhang, K. Huang, L. Yuan, S. Feng, Mineralizer effect on facet-controllable hydrothermal crystallization of perovskite structure YbFeO3 crystals, Crystengcomm 20 (2018) 470–476.
[25] N. Lasemi, O. Bomati Miguel, R. Lahoz, V.V. Lennikov, U. Pacher, C. Rentenberger, W. Kautek, Laser-assisted synthesis of colloidal FeWxOy and Fe/FexOy nanoparticles in water and ethanol, Chemphyschem 19 (2018) 1414–1419.
[26] A. Naghilou, O. Bomati-Miguel, A. Subotic, R. Lahoz, M. Kitzler-Zeiler, C. Radtke, M.A. Rodriguez, W. Kautek, Femtosecond laser generation of bimetallic oxide nanoparticles with potential X-ray absorbing and magnetic functionalities for medical imaging applications, Ceram. Int. 47 (2021) 29363–29370.
[27] C.L. Sajti, R. Sattari, B.N. Chichkov, S. Barcikowski, Gram scale synthesis of pure ceramic nanoparticles by laser ablation in liquid, J. Phys. Chem. C 114 (2010) 2421–2427.

[28] A. Al-Kattan, Y.V. Ryabchikov, T. Baati, V. Chirvony, J.F. Sachez-Royo, M. Sentis, D. Braguer, V.Y. Timoshenko, M.A. Esteve, A.V. Kabashin, Ultrapure laser-synthesized Si nanoparticles with variable oxidation states for biomedical applications, J. Mater. Chem. B 4 (2016) 7852–7858.
[29] V. Amendola, A. Guadagnini, S. Agnoli, D. Badocco, P. Pastore, G. Fracasso, M. Gerosa, F. Vurro, A. Busato, P. Marzola, Polymer-coated silver-iron nanoparticles as efficient and biodegradable MRI contrast agents, J. Colloid Interface Sci. 596 (2021) 332–341.
[30] V. Torresan, D. Forrer, A. Guadagnini, D. Badocco, P. Pastore, M. Casarin, A. Selloni, D. Coral, M. Ceolin, M.B.F. van Raap, A. Busato, P. Marzola, A. E. Spinelli, V. Amendola, 4D Multimodal Nanomedicines Made of Nonequilibrium Au-Fe Alloy Nanoparticles, ACS Nano 14 (2020) 12840–12853.
[31] I.S. Pavlov, E.V. Barmina, M.I. Zhilnikova, G.A. Shafeev, P.V. Zinin, V.P. Filonenko, A.L. Vasiliev, Production of spherical boron-carbide particles encapsulated in a graphite shell, Nanobiotechnol. Rep. 17 (2022) 290–296.
[32] R. Lahoz, E. Natividad, A. Mayoral, C. Rentenberger, D. Diaz-Fernandez, E.J. Felix, L. Soriano, W. Kautek, O. Bomati-Miguel, Pursuit of optimal synthetic conditions for obtaining colloidal zero-valent iron nanoparticles by scanning pulsed laser ablation in liquids, J. Ind. Eng. Chem. 81 (2020) 340–351.
[33] H. Zeng, X.-W. Du, S.C. Singh, S.A. Kulinich, S. Yang, J. He, W. Cai, Nanomaterials via laser ablation/irradiation in liquid: a review, Adv. Funct. Mater. 22 (2012) 1333–1353.
[34] E. Felix, J.M. Mánuel, R. Litrán, M.A. Rodríguez, S. Román-Sánchez, R. Lahoz, E. Natividad, C. Fernández-Ponce, F. Garcia-Cozar, M.J.C.I. Llaguno-Munive, Scanning pulsed laser ablation in liquids: An alternative route to obtaining biocompatible YbFe nanoparticles as multiplatform contrast agents for combined MRI and CT imaging 49, 2023, pp. 9324–9337.
[35] S.S. Davis, E. Inst Mech, Nanoparticles for drug delivery, in: 150th Anniversary Symposium of the Institution-of-Mechanical-Engineers on Visions of Tomorrow - Improving the Quality of Life Through TechnologyLondon, England, 1997, pp. 83–92.
[36] M. Shringirishi, S.K. Prajapati, A. Mahor, S. Alok, P. Yadav, A. Verma, Gold nanoparticles: promising and potential nanomaterial, Int. J. Pharm. Sci. Res. 4 (2013) 4068–4082.
[37] C. Fernandez-Ponce, J.M. Manuel, R. Fernandez-Cisnal, E. Felix, J. Beato-Lopez, J. P. Munoz-Miranda, A.M. Beltran, A.J. Santos, F.M. Morales, M.P. Yeste, O. Bomati-Miguel, R. Litran, F. Garcia-Cozar, Superficial characteristics and functionalization effectiveness of non-toxic glutathione-capped magnetic, fluorescent, metallic and hybrid nanoparticles for biomedical applications, Metals 11 (2021).
[38] C. Fernandez-Ponce, J.P. Munoz-Miranda, D.M. De Los Santos, E. Aguado, F. Garcia-Cozar, R. Litran, Influence of size and surface capping on photoluminescence and cytotoxicity of gold nanoparticles, J. Nanopart. Res. 20 (2018).
[39] I. Pastoriza-Santos, L.M. Liz-Marzan, Reliable methods for silica coating of Au nanoparticles, in: P. Bergese, K. HamadSchifferli (Eds.), Nanomaterial Interfaces in Biology: Methods and Protocols, 2013, pp. 75–93.
[40] A.G. Roca, R. Costo, A.F. Rebolledo, S. Veintemillas-Verdaguer, P. Tartaj, T. Gonzalez-Carreno, M.P. Morales, C.J. Serna, Progress in the preparation of magnetic nanoparticles for applications in biomedicine, J. Phys. D-Appl. Phys. 42 (2009).
[41] A. Chakraborty, M.M. Stanley, B. Mondal, M. Bodiuzzaman Nonappa, P. Chakraborty, M.P. Kannan, T. Pradeep, Tunable reactivity of silver nanoclusters: a facile route to synthesize a range of bimetallic nanostructures, Nanoscale 15 (2023) 2690–2699.
[42] P. Ilg, Simulating the flow of interacting ferrofluids with multiparticle collision dynamics, Phys. Rev. E 106 (2022).
[43] J. van Embden, S. Gross, K.R. Kittilstved, E. Della Gaspera, Colloidal approaches to zinc oxide nanocrystals, Chem. Rev. 123 (1) (2022) 271–326.
[44] M. Nikzamir, A. Akbarzadeh, Y. Panahi, An overview on nanoparticles used in biomedicine and their cytotoxicity, J. Drug Deliv. Sci. Technol. 61 (2021).
[45] R.I. Felimban, H.H. Tayeb, A.G. Chaudhary, M.A. Felemban, F.H. Alnadwi, S.A. Ali, J.A. Alblowi, E. Alfayez, D. Bukhary, M. Alissa, S.H. Qahl, Utilization of a nanostructured lipid carrier encapsulating pitavastatin-Pinus densiflora oil for enhancing cytotoxicity against the gingival carcinoma HGF-1 cell line, Drug Deliv. 30 (2023) 83–96.
[46] J.J. Beato-Lopez, M. Dominguez, M. Ramirez-del-Solar, R. Litran, Glutathione-magnetite nanoparticles: synthesis and physical characterization for application as MRI contrast agent, Sn Appl. Sci. 2 (2020).
[47] A.M. Beltran, J.M. Manuel, R. Litran, E. Felix, A.J. Santos, F.M. Morales, O. Bomati-Miguel, (S)TEM structural and compositional nanoanalyses of chemically synthesized glutathione-shelled nanoparticles, Appl. Nanosci. 10 (2020) 2295–2301.
[48] J.J. Beato-Lopez, M.L. Espinazo, C. Fernandez-Ponce, E. Blanco, M. Ramirez-del-Solar, M. Dominguez, E. Garcia-Cozar, R. Litran, CdTe quantum dots linked to glutathione as a bridge for protein crosslinking, J. Lumin. 187 (2017) 193–200.
[49] J.J. Beato-Lopez, C. Fernandez-Ponce, E. Blanco, C. Barrera-Solano, M. Ramirez-del-Solar, M. Dominguez, F. Garcia-Cozar, R. Litran, Preparation and characterization of fluorescent CdS quantum dots used for the direct detection of GST fusion proteins regular paper, Nanomater. Nanotechnol. 2 (2012).
[50] F. Lu, O. Gang, DNA functionalization of nanoparticles, in: Y. Ke, P. Wang (Eds.), 3d DNA Nanostructure: Methods and Protocols, 2017, pp. 99–107.
[51] J.R. Nicol, D. Dixon, J.A. Coulter, Gold nanoparticle surface functionalization: a necessary requirement in the development of novel nanotherapeutics, Nanomedicine 10 (2015) 1315–1326.
[52] C. Wang, F. Sun, G. He, H. Zhao, L. Tian, Y. Cheng, G. Li, Noble metal nanoparticles meet molecular cages: a tale of integration and synergy, Curr. Opin. Colloid Interface Sci. 63 (2023).
[53] Y. Gao, K. Wang, J. Zhang, X. Duan, Q. Sun, K. Men, Multifunctional nanoparticle for cancer therapy, Medcomm 4 (2023).
[54] Y. Niu, R. Zhang, J. Dong, Z. Pan, H. Wang, Organic dyestuff modifier enhancing energy storage performance of PEI-based nanocomposites, Mater. Lett. 333 (2023).
[55] R. Deshmukh, M. Niederberger, Mechanistic aspects in the formation, growth and surface functionalization of metal oxide nanoparticles in organic solvents, chemistry-a, Eur. J. 23 (2017) 8542–8570.
[56] H.J. Eom, J. Choi, p38 MAPK activation, DNA damage, cell cycle arrest and apoptosis as mechanisms of toxicity of silver nanoparticles in Jurkat T cells, Environ. Sci. Technol. 44 (2010) 8337–8342.
[57] C. Hanley, J. Layne, A. Punnoose, K.M. Reddy, I. Coombs, A. Coombs, K. Feris, D. Wingett, Preferential killing of cancer cells and activated human T cells using ZnO nanoparticles, Nanotechnology 19 (2008).
[58] N. Kimizuka, K. Kato, I. Shindo, I. Kawada, T. Katsura, New compounds of YB3FE4O10 and YB4FE5O13/5O-13, Acta Crystallogr. Sect. B-Struct. Sci. 32 (1976) 1620–1621.
[59] S. Hosokawa, H.-J. Jeon, M. Inoue, Thermal stabilities of hexagonal and orthorhombic YbFeO3 synthesized by solvothermal method and their catalytic activities for methane combustion, Res. Chem. Intermed. 37 (2011) 291–296.
[60] International Centre for Diffraction Data, Powder Diffraction FileTM (PDF®) 2018-2019 (n.d.) File PDF 29-0738, 2023.
[61] International Centre for Diffraction Data, Powder Diffraction FileTM (PDF®) 2018-2019 (n.d.) File PDF 34-1197, 2023.
[62] International Centre for Diffraction Data, Powder Diffraction FileTM (PDF®) 2018–2019 (n.d.) File PDF43–1037, 2023.
[63] International Centre for Diffraction Data, Powder Diffraction FileTM (PDF®) 2018-2019 (n.d.) File PDF 39-0238, 2023.
[64] International Centre for Diffraction Data, Powder Diffraction FileTM (PDF®) 2018-2019 (n.d.) File PDF 39-1346, 2023.
[65] M.H. Mahdieh, B. Fattahi, Size properties of colloidal nanoparticles produced by nanosecond pulsed laser ablation and studying the effects of liquid medium and laser fluence, Appl. Surf. Sci. 329 (2015) 47–57.
[66] D. Zhang, B. Goekce, S. Barcikowski, Laser synthesis and processing of colloids: fundamentals and applications, Chem. Rev. 117 (2017) 3990–4103.
[67] G. Liu, D.-Q. Feng, Y. Qian, W. Wang, J.-J. Zhu, Construction of FRET biosensor for off-on detection of lead ions based on carbon dots and gold nanorods, Talanta 201 (2019) 90–95.
[68] H. Hong, S. Lee, T. Kim, M. Chung, C. Choi, Surface modification of the polyethyleneimine layer on silicone oxide film via UV radiation, Appl. Surf. Sci. 255 (2009) 6103–6106.